Geophysical imaging of the deep critical zone architecture reveals the complex interplay between hydrological and weathering processes in a volcanic tropical catchment

Sylvain Pasquet[1], Jean Marçais[2], Jorden L Hayes[3], Peter Sak[3], Lin Ma[4], and Jerome Gaillardet[5]

[1]Institut de physique du globe de Paris
[2]INRAE
[3]Dickinson College
[4]University of Texas at El Paso
[5]Institut de Physique du Globe Paris (IPGP), France

November 24, 2022

Abstract

The Critical Zone (CZ) evolves through weathering and erosion processes that shape landscapes and control the availability and quality of natural resources. Although many of these processes take place in the deep CZ ($\sim$10-100 m), direct information about its architecture remain scarce. Near-surface geophysics offer cost-effective and minimally-intrusive alternatives to drilling that can provide information about the physical properties of the CZ. We propose a novel workflow combining geophysics, petrophysics and geostatistics to characterize the architecture of the CZ (i.e., weathering front and water table depths) at the catchment scale, on the volcanic tropical island of Basse-Terre (Guadeloupe, France). Our results highlight two spatial organizations patterns for the weathering front and the water table, one along the stream and one transverse to it. This illustrates the robustness and strong potential of the proposed workflow to study hydrological and weathering processes in the CZ.

Geophysical imaging of the deep critical zone architecture reveals the complex interplay between hydrological and weathering processes in a volcanic tropical catchment

Sylvain Pasquet[1], Jean Marçais[2], Jorden L. Hayes[3], Peter B. Sak[3,4], Lin Ma[5], Jérôme Gaillardet[1]

[1]Université de Paris, Institut de physique du globe de Paris, CNRS, Paris, France
[2]INRAE, UR RiverLy, Villeurbanne, France
[3]Department of Earth Sciences, Dickinson College, Carlisle PA, USA
[4]Earth and Environmental Systems Institute and Department of Geosciences, Pennsylvania State University, University Park, PA, USA
[5]University of Texas at El Paso, El Paso TX, USA

Key Points:

- A novel combination of geophysics, petrophysics and geostatistics is used to characterize the architecture of the deep critical zone.
- Maps of regolith thickness and water table depth reveal a deeply weathered zone that impacts the hydrologic functioning of the watershed.
- We highlight spatial organization patterns that call for going beyond "simple" hillslope representations of the CZ.

Corresponding author: Sylvain Pasquet, `pasquet@ipgp.fr`

Abstract

The Critical Zone (CZ) evolves through weathering and erosion processes that shape landscapes and control the availability and quality of natural resources. Although many of these processes take place in the deep CZ (∼10-100 m), direct information about its architecture remain scarce. Near-surface geophysics offer cost-effective and minimally-intrusive alternatives to drilling that can provide information about the physical properties of the CZ. We propose a novel workflow combining geophysics, petrophysics and geostatistics to characterize the architecture of the CZ (i.e., weathering front and water table depths) at the catchment scale, on the volcanic tropical island of Basse-Terre (Guadeloupe, France). Our results highlight two spatial organizations patterns for the weathering front and the water table, one along the stream and one transverse to it. This illustrates the robustness and strong potential of the proposed workflow to study hydrological and weathering processes in the CZ.

1 Introduction

In the Anthropocene, human activities have become a major component of the Earth system, directly affecting the ecosystem services essential to the development of our societies. These services are mostly hosted within the Critical Zone (CZ), which extends from the lower atmosphere to the top of unweathered bedrock (NRC, 2001). The CZ evolves through physical, chemical, and biological weathering and erosion processes that shape landscapes and control the availability and quality of natural resources (Brantley et al., 2007). Many of these processes take place in the deeper parts of the CZ (∼10-100 m), involving complex interactions between rock, air, water and life (Rempe & Dietrich, 2018). The deep CZ is frequently described as a bottom-up sequence of increasingly weathered materials (Riebe et al., 2017). As bedrock is exhumed towards the surface, the release of stress (tectonic or topographic) leads to the opening of fractures (St. Clair et al., 2015) and the exposure of new primary minerals (e.g., feldspar and mica) (Ackerer et al., 2021). These fractures open and connect towards the surface, thus increasing porosity (Hayes et al., 2019; Callahan et al., 2020) and favoring infiltration of reactive meteoric waters and chemical weathering of the rock (Lebedeva & Brantley, 2020; Brantley & Lebedeva, 2021). Besides, channel incision produces lateral drainage of subsurface water, enhancing weathering through drying and oxidation of the top of the CZ (Rempe & Dietrich, 2014). Around the water table, higher concentrations of dissolved O_2 and CO_2 promote dissolution and oxidation reactions which consume primary minerals and release mineral nutrients (Gu, Rempe, et al., 2020; Gu, Heaney, et al., 2020). As weathering intensifies, the bedrock material loses much of its mechanical strength and turns into saprolite, a friable layer yet physically intact enough to retain the texture of the parent bedrock (Graham et al., 2010). Close to the surface, the precipitation of new, less soluble secondary phases (clays, oxides...) and the weakening of the rock structure through bioturbation processes eventually lead to the formation of soils (Wilford & Thomas, 2013). Saprolite and soil are commonly associated into a common unit called regolith (Anderson et al., 2011).

The formation of regolith, and its removal by erosion processes, shapes the structure of the deep CZ (i.e., regolith thickness, porosity and permeability) (Rempe & Dietrich, 2014). This structure in turns impacts groundwater storage, residence time and flow paths (Flinchum, Holbrook, Grana, et al., 2018; Kolbe et al., 2020). It is strongly linked to many socially-relevant issues, including flooding and run-off (Lana-Renault et al., 2007; Guérin et al., 2019) which affect slope stability (Nevers et al., 2021). The depth of the water table is also tightly intertwined with the structure of the deep CZ (Wang et al., 2021). Its monitoring is essential to manage groundwater resource (Carrière et al., 2018) and quality (Turkeltaub et al., 2020). Agricultural practices also strongly depend on this deep compartment, as it controls river base-flow (Hector et al., 2015), exchanges in the hyporheic zone (Floury et al., 2019), crop yield (Mahindawansha et al., 2018), rooting depth (Shi et al., 2021), diversity of microorganisms (Stumpp & Hose, 2013), and organic matter accumulation or leaching (Jeanneau et al., 2020). Water table levels also control the sustainability of wetlands (Bertrand et al., 2021), and at a larger scales directly impact climate through their connection to soil moisture and carbon storage across continents (Fan et al., 2013). Despite these motivations, our understanding of mechanisms controlling these processes remains limited by the difficulty of accessing the CZ at depth. Boreholes and piezometric wells are often used to image the architecture of the CZ and locate the water table, but data remain limited by costs, field access, spatial coverage and the destructive nature of such measurements (Hubbard & Linde, 2011; Maillot et al., 2019; Holbrook et al., 2019).

Minimally-invasive surface-based geophysical methods can be used to fill spatial gaps between wells by producing higher lateral resolution and lower cost data (Hubbard & Linde, 2011; Parsekian et al., 2015). Over the past ten years, an increasing number of studies have used geophysical methods to characterize the architecture of the CZ (Olona et al., 2010; Befus et al., 2011; Pasquet, Bodet, Longuevergne, et al., 2015; St. Clair et al., 2015; Yaede et al., 2015; Orlando et al., 2016; Novitsky et al., 2018; Comas et al., 2019; Eppinger et al., 2021; Parsekian et al., 2021; Wang et al., 2021, 2022). The vast majority of these studies rely on seismic refraction tomography to estimate pressure-wave velocity (V_P) at the hillslope scale. This observable is sensitive to subsurface mechanical properties which vary according to changes of porosity, bulk density or water content (Pride, 2005). To disentangle the cumulative effects of these parameters, a growing number of studies have used petrophysical relationships so as to convert these geophysical measurements into quantitative estimates of subsurface properties (Holbrook et al., 2014; Flinchum, Holbrook, Rempe, et al., 2018; Gase et al., 2018; Callahan et al., 2020). In most cases, the authors assume dry subsurface conditions to estimate porosity, and do not take into account variations of water content in the vicinity of the water table. The water content information is often obtained by relying on additional geophysical or piezometric data (Linde et al., 2007; Buchanan & Triantafilis, 2009; Boucher et al., 2009; Hayes et al., 2019; Flinchum et al., 2019). Several recent studies have shown that information about the water content could be inferred by estimating shear wave velocity (V_S) along with V_P (Grelle & Guadagno, 2009; Pasquet, Bodet, Dhemaied, et al., 2015; Pasquet, Bodet, Longuevergne, et al., 2015; Flinchum et al., 2020). Indeed, V_S is by definition less sensitive to changes in water content (Biot, 1956a, 1956b), since shear waves do not propagate in fluids. Combining both velocities in a petrophysical inversion framework thus allows reducing the ambiguity between lithological and water content variations at depth. This approach, previously implemented to characterize shallow hydrothermal activity in Yellowstone (WY) (Pasquet et al., 2016), is applied here for the first time to study CZ processes.

We propose a novel workflow combining geophysics, petrophysics and geostatistics to characterize the catchment scale CZ architecture, namely its vertical weathering structure and its related water table position. We apply this framework on the volcanic tropical island of Basse-Terre (Guadeloupe, France). We process seismic data collected along 5 different profiles in a small (8 ha) forested watershed. For each of these profiles, we combine seismic refraction tomography (SRT) and multichannel analysis of surface waves (MASW) to simultaneously estimate V_P and V_S velocities from a single seismic data set. Using the petrophysical inversion framework presented by Pasquet et al. (2016), we then convert these velocities into spatial distributions of subsurface porosity and saturation. Both V_P and saturation values are used to characterize the vertical structure of the CZ and the water table position in the watershed. We then use ordinary kriging interpolation to produce subsurface maps of the weathering front and the water table across the entire catchment. The spatial distribution of the regolith thickness and the water table depth reveal a deeply weathered zone that consistently impacts the hydrologic functioning of this tropical watershed. Overall this study highlights the potential of this novel workflow to investigate reactive and hydrological processes in the CZ with cost-effective, minimally-intrusive geophysical methods.

2 Site Description

The Quiock Creek watershed is a 8 ha headwater catchment located on the windward side of Basse-Terre Island, the volcanic part of the Guadeloupe archipelago (France) in the Lesser Antilles (Figure 1). The catchment is monitored by the ObsErA observatory which is part of the OZCAR critical zone research infrastructure (Gaillardet et al., 2018) and is dedicated to the study of weathering and erosion processes in the CZ under tropical climates (Clergue et al., 2015; Guérin et al., 2019; Dessert et al., 2015, 2020). Indeed, due the volcanic nature of the rock formations and the tropical climate of Guadeloupe, weathering rates (i.e., the rate of transformation of rock into saprolite and soil) are amongst the highest on the planet (Gaillardet et al., 2011). The Quiock catchment is fully representative of volcanic tropical landscapes which are known to be hotspots of nutrient production, biological productivity and soil CO_2 consumption by chemical weathering (Louvat & Allègre, 1997; Dessert et al., 2001). The Quiock Creek is a small trib-

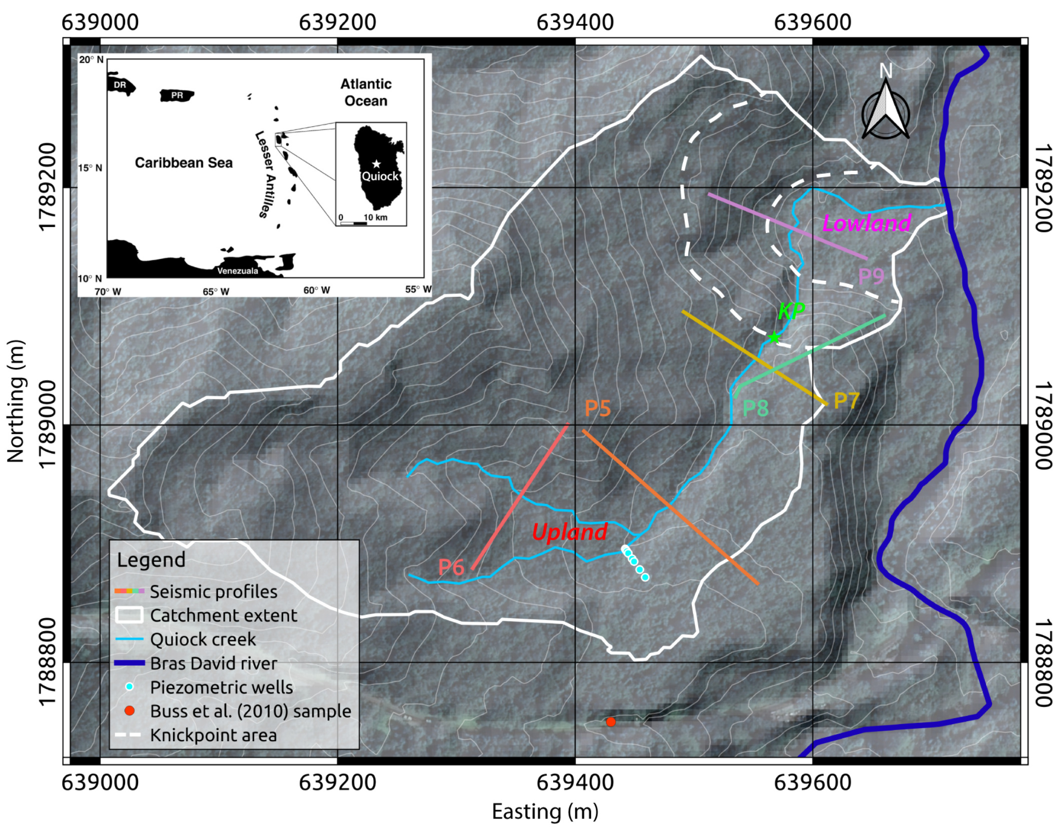

Figure 1. Topographic map of the studied area with 5-m elevation contours, showing the extent of the Quiock Creek watershed (white line) and the hydrological network (blue lines). Seismic profiles (colored lines), piezometric wells (light blue dots) and direct samples from Buss et al. (2010) (red dot) are also represented. The knickpoint area is delineated with dashed white line, and its location along the stream is shown with a green star. This map, and the following, are projected in the Universal Transverse Mercator geographic coordinate system, zone 20 N. The top left inset shows the location of Basse-Terre island in the Lesser Antilles.

utary of the Bras David river and is located in the primary tropical rainforest of Guadeloupe National Park with mean annual temperature of 25°C. The elevation of the catchment ranges from 200 m to 350 m and includes an active river knickpoint (i.e., sharp convexity in an otherwise concave-up longitudinal river profile). The knickpoint is located at ∼250 m upstream of the confluence with the Bras David river and separates regionally extensive low relief surface upstream of the knickpoint, from more deeply incised streams downstream (Sak et al., 2018). The hydrology of the site is strongly influenced by tropical storms and hurricanes, with mean annual precipitation of 3500 mm/yr, evapotranspiration between 60 and 70%, and runoff of 1130 mm/yr (Dessert et al., 2020). Water table levels are continuously monitored upstream of the knickpoint with pressure transducers installed in 7 piezometric wells arranged along a 30-m linear transect perpendicular to the stream (Figure 1) and vary between 0.1 m and 4.1 m in the farthest well. The catchment lies within Pleistocene andesitic pyroclastic deposits (Boudon et al., 1988) that are weathered into a very thick regolith profile with ferralitic soils at the surface (Buss et al., 2010). This weathering profile is highly depleted in mobile elements (Clergue et al., 2015) and is mainly constituted of secondary minerals, with about 66% clay (halloysite and kaolinite) and 28% iron and aluminum hydroxides (magnetite, goethite, maghemite and gibbsite), minor amounts of primary minerals (mostly quartz and cristobalite) making up the rest of the regolith composition. Bulk density measured in auger samples in the upper 5 m is particularly low, on average ∼1 g.cm^{-3} (Buss et al., 2010).

3 Material and Methods

3.1 Seismic Data Acquisition and Processing

Seismic data were first collected in May 2016 along a 188-m-long profile (P5) crossing the Quiock Creek near the piezometric wells (Figure 1). Four supplemental 142-m-long profiles (P6 to P9) were collected in May 2019, both up and downstream from the original P5 transect. For each profile, P-wave first arrival times were picked manually, then inverted for subsurface P-wave velocity (V_P) structure using the seismic refraction tomography (SRT) code included in the Python geophysical inversion and modelling library pyGIMLI (Rücker et al., 2017). The program starts with an initial 2D model consisting of a velocity field that increases linearly with depth, and then finds an appropriately smooth update to the model that reduces the difference between predicted and observed traveltimes (more details in the supporting information). These traveltimes are compared for each source-receiver pair to check the quality of the inversion (Figure S1 in the supporting information). Velocity uncertainties (Figure S2) were estimated by running 144 inversions for each profile, using a different set of starting model and regularization parameters for each inversion run (St. Clair et al., 2015; Pasquet et al., 2016). The 144 inverted models are merged to build an average velocity model describing the V_P distribution at depth along each profile (Figure 2b-2f).

The seismic data were also processed to perform multichannel analysis of surface-waves (MASW) using the SWIP software package (Pasquet & Bodet, 2017). SWIP uses spatial windowing and spectral stacking techniques (Neducza, 2007; O'Neill et al., 2003) to extract surface-wave dispersion data from the seismic records and retrieve a 2D model of shear-wave velocity (V_S) from a succession of 1D inversions. We specifically apply the novel multiwindow weighted stacking of surface-wave procedure (Pasquet et al., 2020) to extract higher quality dispersion data and improve both the lateral resolution and depth of investigation of the models (more details in the supporting information). Dispersion curves are picked manually along each profile, and then inverted using the neighborhood algorithm (NA) with the open software package Geopsy (Wathelet et al., 2004). For each extracted dispersion curve, the NA inversion procedure generates 25000 models which are used to build a 1D misfit-weighted final V_S model. The overall quality of these inversions is quantified by computing the residuals between observed and calculated dispersion curves along each profile (Figure S3). For each profile, all the consecutive 1D V_S

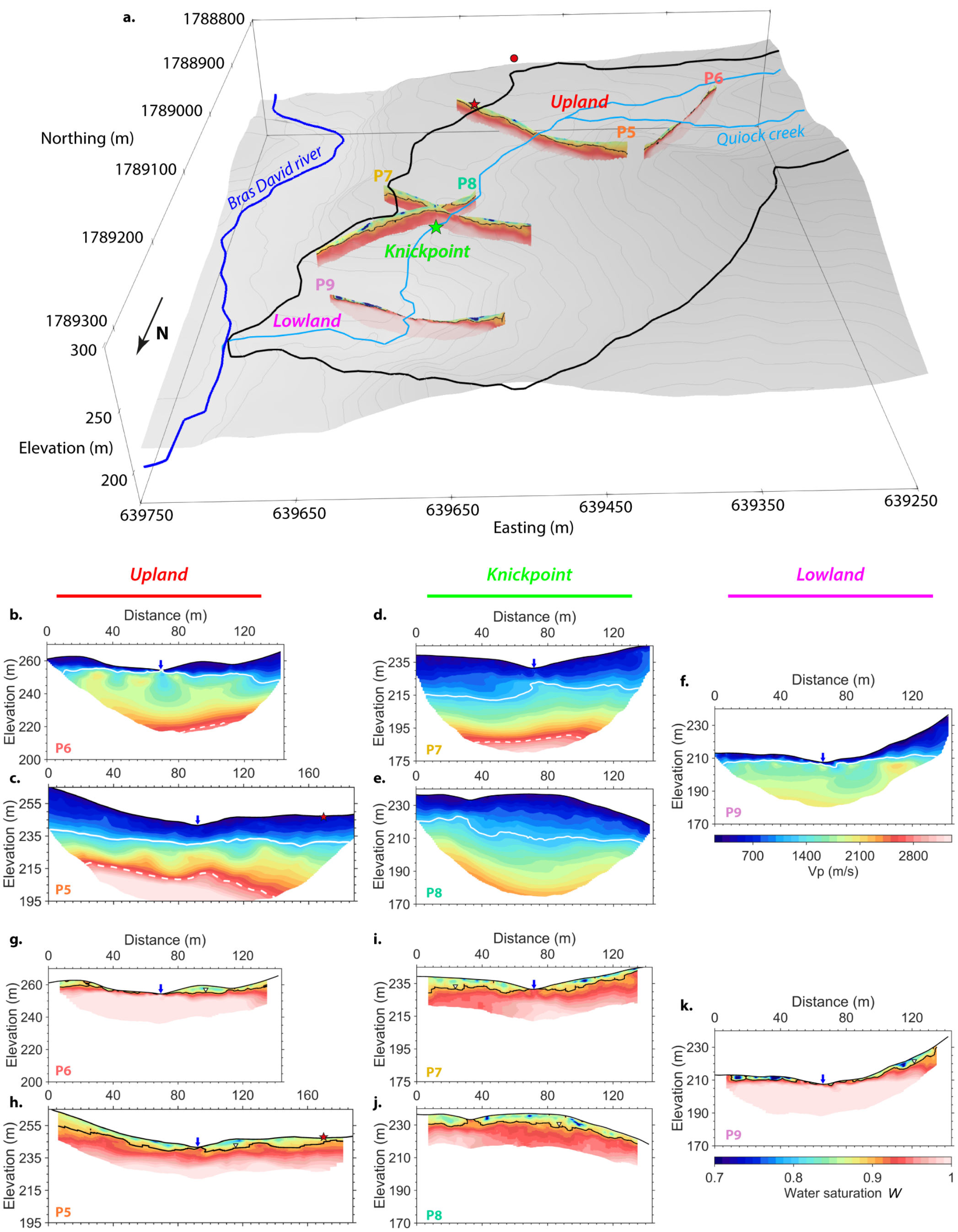

Figure 2. (a) 3D view of the inferred subsurface water saturation profiles in the Quiock catchment. The hydrological network (blue lines), the extent of the watershed (black line) and the location of the knickpoint (green star) are also represented. (b–f) P-wave velocity V_P and (g-k) water saturation profiles, with the blue arrows indicating the location of the stream. Horizontal distance = 0 m corresponds to the label position in (a). V_P contours corresponding to the bottom of saprolite (1200 m/s, white solid line) and the transition between weathered and fractured bedrock (2700 m/s, white dashed line) are shown in (b-f). Black contour lines in (g-k) correspond to the inferred water table ($W = 0.9$). The petrophysical model was calibrated by comparing soil sample analysis from Buss et al. (2010) (red dot in a) with the closest seismic data point at 170 m along P5 (red star in a, c and h).

models are finally assembled to create a 2D V_S section with the depth of investigation estimated from the uncertainties of each NA inversion (Figure S4).

3.2 Petrophysical Inversion

The inversion strategy relies on a petrophysical model based on Hertz-Mindlin contact theory (Mindlin, 1949) that describes the weathered regolith as a pack of spherical beads. This is consistent with the textural description of highly weathered saprolite in tropical volcanic islands (White et al., 1998). With this model, we can express the bulk elastic properties of the regolith (i.e., bulk and shear moduli) as functions of the elastic properties of the minerals and fluids constituting the medium, and of their relative proportions (i.e., mineralogy, porosity and saturation). Here, we assume that all the beads in the model have an identical mineral composition that corresponds to the average composition of the regolith (66% clay, 28% hydroxides and 6% quartz) observed in direct samples collected at the site (Buss et al., 2010). A complete description of the model and the calibration of its parameters is given in the supporting information. The Hertz-Mindlin petrophysical model is then used in a grid search inversion scheme to look for the best set of porosity (Φ) and water saturation (W) values that minimizes the differences between observed and modelled V_P and V_S (Figure S6), considering errors previously estimated with SRT and MASW inversions. The grid search procedure was performed with porosity and saturation ranging between 0 and 1 in every cell of the 5 geophysical profiles presenting valid values of both V_P and V_S. It allowed us to reconstruct 2D sections of porosity (Figure S7) and saturation (Figure 2g-2k), and evaluate their uncertainties (Figure S8).

3.3 Describing the Critical Zone Architecture

The depth of the interfaces between layers within the CZ can be estimated using the results of SRT. St. Clair et al. (2015) have pointed out that fresh bedrock is usually characterized by $V_P > 4000$ m/s, whereas fractured bedrock is expected to have $V_P > 2700$ m/s in volcanic rocks (Adelinet et al., 2018). Several recent studies also described saprolite with $V_P < 1200$ m/s (Flinchum, Holbrook, Rempe, et al., 2018; Hayes et al., 2019). Soils express a large range of V_P which depends on their compaction and saturation levels, but generally show $V_P < 800$ m/s (Santamarina et al., 2005). However, when one of these interfaces lies in the vicinity of the water table, V_P is influenced by variations of subsurface water content and can bias the estimation of the corresponding interface depth (Pasquet, Bodet, Dhemaied, et al., 2015). Here we propose to use the results of the petrophysical inversion to map the depth of the water table and thus unbias the V_P-based estimation of the CZ interfaces. We define the depth of the water table when water saturation reaches a critical value (W_c) of 0.9, which corresponds to the top of the capillary fringe (de Marsily, 1986). We also consider an unbiased V_P-based estimation of a given interface depth as long as it is located below the water table (i.e., in fully saturated conditions).

While we could identify the saprolite-weathered bedrock interface ($V_P = 1200$ m/s) and the water table ($W = 0.9$) along all five seismic profiles collected in the Quiock catchment, the weathered to fractured bedrock interface ($V_P = 2700$ m/s) could only be detected in the three profiles collected upstream of the knickpoint (Figure 2). As the estimated saprolite-weathered bedrock interface is systematically located under the water table (Figure 2), we consider that it is not biased by subsurface water content variations. Soil thickness could not be precisely determined due to the large spacing between geophones (>2 m) used for both seismic campaigns, and is therefore not discussed further. In the following, soil and saprolite are undifferentiated and gathered within regolith. Similarly, the boundary between the bottom of regolith and the top of weathered bedrock is referred to as the weathering front.

3.4 Interpolating the Weathering Front and the Water Table

Since only the weathering front and the water table are clearly identified in all the seismic profiles, we focus the following section solely on reconstructing the 3D shape of these two interfaces across the catchment. We first extracted, from the digital elevation model (DEM) (Figure 3a), the spatial coordinates of these two interfaces at each point along the seismic profiles. We also added boundary conditions in the Bras David river to better constrain the interpolations, assuming: (i) a mean regolith thickness of 2 m that coincides with the most lowland values observed along P9 (Figure 2f), and (ii) a mean water level of 0.5 m, considering that the aquifer is directly connected to the river. We then used the GSTOOLS python library (Müller & Schüler, 2021) to interpolate the weathering front and the water table across the catchment (more details in the supporting information). We specifically applied ordinary kriging along a regular grid of 10x10 m cells covering the entire watershed in order to generate 3D surfaces of both the depth (i.e. vertical distance under the surface) and the elevation (i.e., vertical distance above sea level) of these interfaces. As shown by Snyder (2008), the water table position is better constrained by combining interpolations of both its depth and elevation. The interpolation of the water table elevation is more sensitive to the main trend associated with the regional hydrological gradient, whereas the interpolation of its depth helps reconstructing local perturbations associated with land surface irregularities. Following Snyder (2008), we used the average of these two interpolations to produce a map of the water table depth (Figure 3c) that incorporates both local and regional information. The same strategy was applied to interpolate the depth of the weathering front across the catchment (Figure 3b).

4 Results and Discussion

4.1 Characterization of the Critical Zone Architecture

In the upper 2-12 meters, V_P are mostly < 1200 m/s which is characteristic of clays constituting saprolite in highly weathered terrains such as those on Basse-Terre (Buss et al., 2010). As this 1200 m/s threshold is always located below the estimated water table (Figure 2), we consider that the estimation of the weathering front based on this threshold is not biased by variations of subsurface water content. The seismic data clearly underline a deepening of the weathering front in the knickpoint (Figure 2c-e), in comparison to upland and lowland areas (Figure 2b and 2f, respectively). The interpolated depth of the weathering front (Figure 3b) reveals a similar pattern, with a clear thickening of the regolith (> 15 m) in the vicinity of the knickpoint. In upland and lowland areas, the weathering front is closer to the surface at depths < 5 m. This particular organization is summarized in a synthetic cross-section (Figure 3f) where the depth of each interface identified in the seismic transects is represented along the topographic profile of the Quiock stream at their respective location (i.e., at the intersection or at the closest point in the stream).

The velocity threshold $V_P > 2700$ m/s, associated with the transition zone between weathered bedrock and fractured bedrock, is only reached upstream of the knickpoint (Figure 2b-d), at depths of about 40-50 m. Therefore it could not be interpolated across the whole catchment, and is only interpreted along the synthetic cross-section of the stream (Figure 3f). In the knickpoint (Figure 2e) and downstream of the knickpoint (Figure 2f), V_P is always < 2700 m/s over the whole investigated area, which goes as deep as 50 m in P8. Although we cannot image the base of the weathered bedrock in these areas, these results show that weathered bedrock extends at least down to 45 m in the lower end of the knickpoint, and down to 30 m in lowland areas. As no obvious deepening of the weathered-to-fractured bedrock transition zone is detected, we can hypothesize that this interface is located at a depth of about 40-50 m across the whole catchment, roughly following the landscape surface topography. Intact bedrock, usually described with velocities of 4000 m/s, is never reached in the catchment, and is therefore located at depths > 50 m. Such a thick weathered zone is in good agreement with deep drilling observations made in similar tropical volcanic environment, where saprolite has been observed down to about 40 m (Buss et al., 2013).

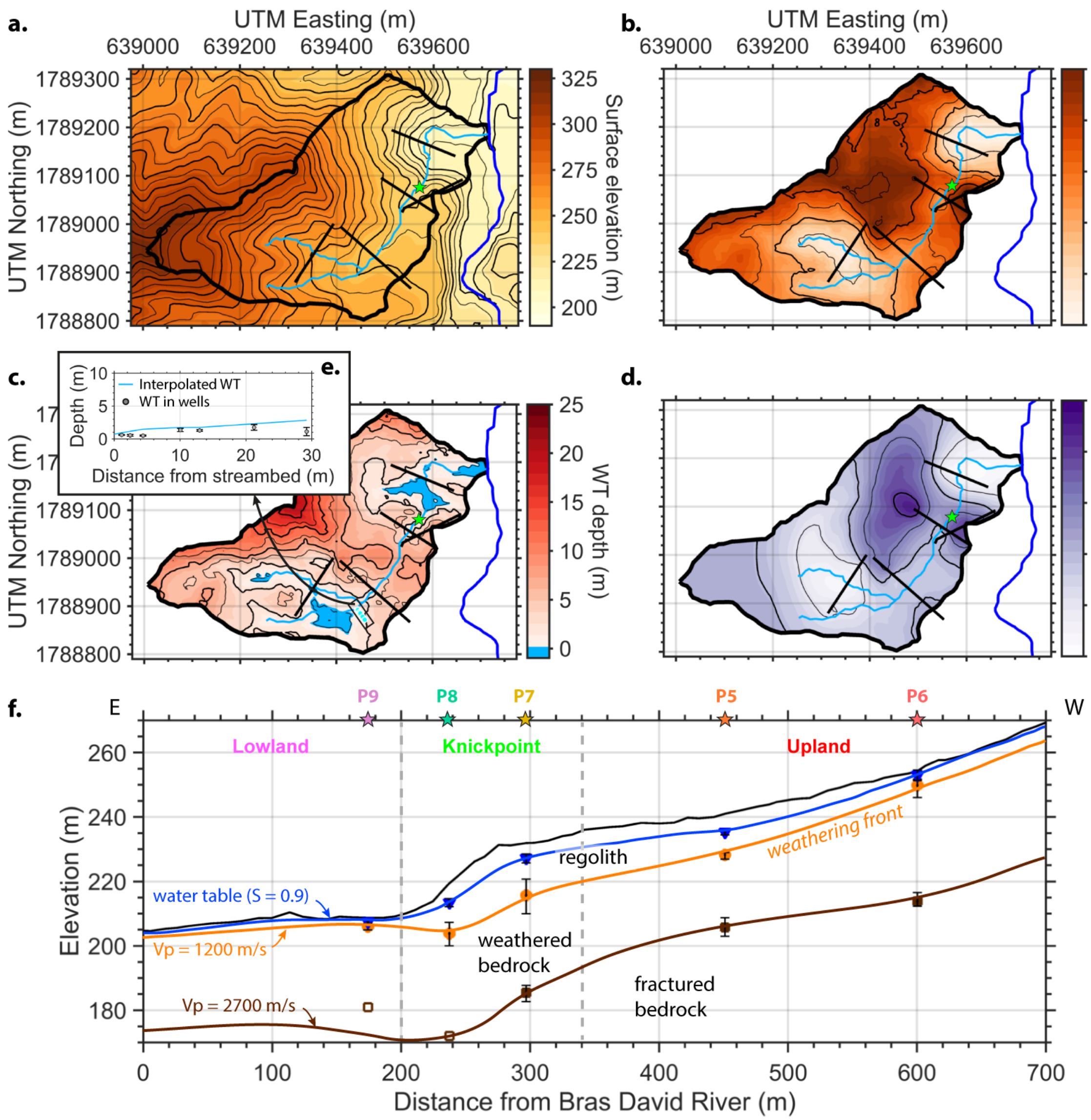

Figure 3. (a) DEM of the Quiock Creek watershed. (b) Interpolated depth of the weathering front (WF). (c) Interpolated depth of the water table (WT). (d) Difference between water table and weathering front elevations. These maps are overlaid with 5-m elevation/depth contours. The extent of the catchment and the seismic lines are shown in black, and the hydrological network in blue. (e) Comparison of average water table levels observed during the geophysical campaign in piezometric wells (light blue dots in c) with the corresponding interpolated water table depths. (f) Interpretive cross section of the stream topographic profile (black line) computed from the 5-m DEM. It highlights the location of the water table (in blue) and displays the structure of the CZ with specific V_P contours describing the weathering front (in orange), and the transition zone between weathered and fractured bedrock (in brown).

Inverted saturation cross sections provide estimates of water table levels that are consistent with field observations. Upstream of the knickpoint (Figure 2g-2i), the estimated water table outcrops at the intersections between the seismic profiles and the stream, in which water was flowing during the field campaign. The water table also outcrops in the small tributary crossed at the southern end of profile P8, whereas it goes deeper (∼10 m) in the knickpoint (Figure 2j). Downstream of the knickpoint, the water table outcrops again widely (Figure 2k) in an area that was saturated during the May 2019 campaign. All these observations are consistent with the expected shape of the free water table in this small tropical catchment (Guérin et al., 2019). Interpolated water table elevations (Figure S10) show a W-E trend that roughly follows the surface elevation gradient (Figure 3a) oriented towards the Bras David river. This illuminates the overarching control that the Bras David river exerts on groundwater flow circulation in the Quiock catchment. Interpolated water table depths (Figure 3c) highlight three main seepage areas: (i) upstream of the knickpoint, before the junction of upper stream branches, (ii) just downstream of the knickpoint, and (iii) near the outlet. The depth to the top of the water table also increases beneath ridges, upstream and in the knickpoint (i.e., between profiles P5 and P7). The estimated levels were compared to those observed in the piezometric wells installed in the catchment (Guérin et al., 2019). The observed water table levels were averaged over periods of one month centered on both field campaigns. These averaged piezometric levels show remarkably good agreement with water table levels interpolated with the average kriging approach (mean absolute error of 0.72 m) (Figure 3e). In comparison, water table levels interpolated solely with the elevations or the depths show significant deviation from the levels observed in piezometric wells (mean absolute errors of 0.74 m and 1.77 m, respectively) (Figure S11), confirming the robustness of the average kriging approach.

4.2 Implications for the Functioning of the Critical Zone

The joint characterization of the subsurface structure and water table depth in this tropical volcanic catchment sheds new light on reactive and hydrological processes governing the functioning of the CZ. It appears that both the groundwater flow circulation and the regolith thickness are significantly impacted by the knickpoint. In upland area, far from the knickpoint, the water table appears to be classically controlled by the topography of the hillslope organization (Haitjema & Mitchell-Bruker, 2005) (Figure 3d-e). There, the water table is the deepest under the hill crest, at the water divide, and then rises up until meeting the land surface in the adjacent river. The weathering front follows the same organization, deeper under the hill crest than at the river ridges, although being always below the water table. On the contrary, just upstream of, and in the knickpoint, the water table and the regolith thickness becomes completely disconnected from the surface, materializing a deepening of groundwater flow circulation concomitant with a thickening of the regolith (Figure 3f). Downstream of the knickpoint, in lowland areas, the water table outcrops in vast saturated areas caused by the resurgence of groundwater flowpaths that originally come from upstream of the knickpoint (Figure 3c), as materialized by the deepening of the water table. In lowland areas, the regolith becomes thinner, between 0 and 5 m. There, a shallow water table is likely to prevent deep infiltration and rather favors shallow subsurface flowpaths, thus hindering regolith development (Weiler et al., 2006; Tromp-van Meerveld & McDonnell, 2006). Overall, the difference between the water table and the weathering front (Figure 3d), appears to be spatially organized along the stream profile (i.e. following the knickpoint) rather than transverse to it (classical hillslope organization).

Two lateral organizations are thus structuring the catchment: one transverse from the hill crest towards the closest stream reach, and one longitudinal from the upland to the lowland area through the knickpoint. Understanding this particular organization, its impact on groundwater circulations, chemical weathering and erosion activity, requires to revisit evolution models coupling hydrology, weathering and erosion (Harman & Cosans, 2019; Braun et al., 2016; Brantley & Lebedeva, 2021). Indeed these hillslope models are intrinsically 2D, considering flowpaths from the hill crest to the river, and are thus unable to simulate the complex 3D hydrological and reactive processes that lead to the CZ organization observed here.

4.3 Limitations and Challenges of the Workflow

A close examination of the petrophysical inversion residuals reveals that velocity distributions observed along P6 and P9 are not well reproduced at depth (Figure S6). This discrepancy is most likely due to the inability of the Hertz-Mindlin petrophysical model to correctly represent seismic velocities in high-velocity and less-weathered materials. Yet, this does not impact our water table level estimates, as these are located above the poorly resolved areas. Another limitation of the modelling approach is the relative lack of studies describing the elastic parameters of secondary minerals that constitute the regolith profile in the Quiock catchment. For instance, we were only able to find a single publication reporting elastic parameters for iron oxides and hydroxides (Chicot et al., 2011). As an alternative, we could collect regolith samples at multiple locations along the seismic lines to estimate the bulk elastic parameters of the dry frame along with porosity and water content (Heap et al., 2021), so as to further constrain the petrophysical model. The proposed workflow could also be improved by collecting additional geophysical data along the existing profiles. Incorporating electrical resistivity data into the petrophysical inversion framework would help constraining variations of clay content across the catchment, as this parameter is especially sensitive to the presence of water and clay, and can be modelled in rocks via Archie's law (Archie, 1942) and its more advanced derivatives (Waxman & Smits, 1968; Glover, 2010; Jougnot et al., 2010).

The quality and robustness of the interpolation is sensitive to the number and density of data points collected throughout the catchment. In this study we were only able to record five seismic profiles with data points unevenly distributed. As a result, the elevations of the weathering front and the water table estimated in the outermost parts of the catchment are rather extrapolated than interpolated and thus only follow the main elevation and depth trends. We assume that the general trend of the elevation gradient used to extrapolate both weathering front and water table levels only remains valid within the catchment, and thus do not display the kriging results beyond the watershed (Figure 3). Improving the density and coverage of data points across the catchment remains challenging in rugged and densely vegetated landscapes. Drilling additional piezometric wells is costly and strictly regulated by Guadeloupe National Park policy. Deploying extra seismic profiles across the catchment would help filling those gaps, yet requiring an improved methodology to optimize acquisition time and spatial coverage.

5 Conclusions

Using a novel combination of geophysics, petrophysics and geostatistics, we provided an extended characterization of the CZ architecture. With a single geophysical survey, we were able to map both the weathering front and the water table in a forested watershed representative of tropical volcanic landscapes in the island of Basse-Terre (Guadeloupe, France). The proposed workflow uses seismic refraction tomography and multichannel analysis of surface waves to retrieve 2D cross sections of P and S wave velocities (V_P and V_S, respectively). While V_P were used to extract information about both the depths of the weathering front and the fractured bedrock, we combined V_P and V_S information in a petrophysical inversion framework to extract saturation values and highlight the position of the water table. We then used a kriging interpolation to infer spatial variation of both the weathering front and the water table across the catchment. The estimated water table levels are consistent with theoretical predictions and field observations. Our results highlight a shallow water table (mostly < 5 m) and relatively thick weathered zone (>15 m) in most parts of the catchment. Both the weathering front and the water table appear to be impacted by the knickpoint and deepen in its vicinity. The top of the fractured bedrock, when shallow enough to be detected, remains parallel to the topography at depths of about 45 m. This integrated view of the CZ architecture also highlights two main spatial organization patterns across the catchment: one transverse, along the hillslope, and one longitudinal, along the stream, strongly impacted by the knickpoint. These findings call for going beyond "simple" hillslope representations of the CZ when studying hydrological and weathering processes in such complex environments. These results also illustrate the robustness and strong potential of the proposed workflow for future critical zone studies.

Acknowledgements

We thank L. Bodet and UMR METIS at Sorbonne Université for lending part of the geophysical equipment, and E. Lajeunesse and the Obsera staff for running and maintaining the observatory's instrumentation and database. We are also grateful to A. Arènes, L. Derry, J. Druhan, M. Eichner, N. Fernandez, C. Le Traon and F. Levy for invaluable assistance during field work. This work was supported by the CRITEX ANR-11-EQPX-0011 project and NSF EAR Award No. 1251952.

Open Research

The seismic data used in this study are available on the H+ database which stores the geophysical data collected on the critical zone observatories of the OZCAR network. The data set can be accessed via `https://doi.org/10.26169/hplus.obsera_seismic_data_2019`.

References

Ackerer, J., Ranchoux, C., Lucas, Y., Viville, D., Clément, A., Fritz, B., . . . Chabaux, F. (2021, November). Investigating the role of deep weathering in critical zone evolution by reactive transport modeling of the geochemical composition of deep fracture water. *Geochimica et Cosmochimica Acta*, *312*, 257–278. Retrieved from https://www.sciencedirect.com/science/article/pii/S001670372100435X doi: 10.1016/j.gca.2021.07.017

Adelinet, M., Domínguez, C., Fortin, J., & Violette, S. (2018, January). Seismic-refraction field experiments on Galapagos Islands: A quantitative tool for hydrogeology. *Journal of Applied Geophysics*, *148*, 139–151. Retrieved from http://www.sciencedirect.com/science/article/pii/S092698511730037X doi: 10.1016/j.jappgeo.2017.10.009

Anderson, S. P., Anderson, R. S., Hinckley, E.-L. S., Kelly, P., & Blum, A. (2011, June). Exploring weathering and regolith transport controls on Critical Zone development with models and natural experiments. *Applied Geochemistry*, *26*, S3–S5. Retrieved from http://www.sciencedirect.com/science/article/pii/S088329271100093X doi: 10.1016/j.apgeochem.2011.03.014

Archie, G. (1942, December). The Electrical Resistivity Log as an Aid in Determining Some Reservoir Characteristics. *Transactions of the AIME*, *146*(01), 54–62. Retrieved from https://doi.org/10.2118/942054-G doi: 10.2118/942054-G

Befus, K. M., Sheehan, A. F., Leopold, M., Anderson, S. P., & Anderson, R. S. (2011, August). Seismic Constraints on Critical Zone Architecture, Boulder Creek Watershed, Front Range, Colorado. *Vadose Zone Journal*, *10*(3), 915–927. Retrieved from https://dl.sciencesocieties.org/publications/vzj/abstracts/10/3/915?search-result=1 doi: 10.2136/vzj2010.0108

Bertrand, G., Ponçot, A., Pohl, B., Lhosmot, A., Steinmann, M., Johannet, A., … Toussaint, M.-L. (2021, February). Statistical hydrology for evaluating peatland water table sensitivity to simple environmental variables and climate changes application to the mid-latitude/altitude Frasne peatland (Jura Mountains, France). *Science of The Total Environment*, *754*, 141931. Retrieved from `https://www.sciencedirect.com/science/article/pii/S0048969720354607` doi: 10.1016/j.scitotenv.2020.141931

Biot, M. A. (1956a, February). Theory of propagation of elastic waves in a fluid-saturated porous solid. II. Higher frequency range. *The Journal of the Acoustical Society of America*, *28*(2), 179–191. Retrieved from `http://link.aip.org/link/?JAS/28/179/1` doi: 10.1121/1.1908241

Biot, M. A. (1956b, January). Theory of propagation of elastic waves in a fluid-saturated porous solid. I. Low-frequency range. *The Journal of the Acoustical Society of America*, *28*(2), 168–178. Retrieved from `http://adsabs.harvard.edu/abs/1956ASAJ...28..168B` doi: 10.1121/1.1908239

Boucher, M., Favreau, G., Descloitres, M., Vouillamoz, J.-M., Massuel, S., Nazoumou, Y., … Legchenko, A. (2009, October). Contribution of geophysical surveys to groundwater modelling of a porous aquifer in semiarid Niger: An overview. *Comptes Rendus Geoscience*, *341*(10), 800–809. Retrieved from `http://www.sciencedirect.com/science/article/pii/S1631071309001680` doi: 10.1016/j.crte.2009.07.008

Boudon, G., Dagain, J., Demet, M.-P., & Wetsercamp, D. (1988). *Notice explicative et carte géologique à 1/20 000 du Massif Volcanique de la Soufrière* (BRGM-CNRS- DRM-IPGP ed.).

Brantley, S. L., Goldhaber, M. B., & Ragnarsdottir, K. V. (2007, October). Crossing Disciplines and Scales to Understand the Critical Zone. *Elements*, *3*(5), 307–314. Retrieved from `https://pubs.geoscienceworld.org/elements/article-abstract/3/5/307/137740/Crossing-Disciplines-and-Scales-to-Understand-the` doi: 10.2113/gselements.3.5.307

Brantley, S. L., & Lebedeva, M. I. (2021). Relating land surface, water table, and weathering fronts with a conceptual valve model for headwater catchments. *Hydrological Processes*, *35*(2), e14010. Retrieved from `http://onlinelibrary.wiley.com/doi/abs/10.1002/hyp.14010` (_eprint: https://onlinelibrary.wiley.com/doi/pdf/10.1002/hyp.14010) doi: https://doi.org/10.1002/hyp.14010

Braun, J., Mercier, J., Guillocheau, F., & Robin, C. (2016). A simple model for regolith formation by chemical weathering. *Journal of Geophysical Research: Earth Surface*, *121*(11), 2140–2171. Retrieved from `https://agupubs.onlinelibrary.wiley.com/doi/abs/10.1002/2016JF003914` doi: 10.1002/2016JF003914

Buchanan, S., & Triantafilis, J. (2009). Mapping Water Table Depth Using Geophysical and Environmental Variables. *Groundwater*, *47*(1), 80–96. Retrieved from `http://ngwa.onlinelibrary.wiley.com/doi/abs/10.1111/j.1745-6584.2008.00490.x` (_eprint: https://onlinelibrary.wiley.com/doi/pdf/10.1111/j.1745-6584.2008.00490.x) doi: 10.1111/j.1745-6584.2008.00490.x

Buss, H. L., Brantley, S. L., Scatena, F. N., Bazilievskaya, E. A., Blum, A., Schulz, M., … Cole, D. (2013). Probing the deep critical zone beneath the Luquillo Experimental Forest, Puerto Rico. *Earth Surface Processes and Landforms*, *38*(10), 1170–1186. Retrieved from `http://onlinelibrary.wiley.com/doi/abs/10.1002/esp.3409` (_eprint: https://onlinelibrary.wiley.com/doi/pdf/10.1002/esp.3409) doi: 10.1002/esp.3409

Buss, H. L., White, A. F., Dessert, C., Gaillardet, J., Blum, A. E., & Sak, P. B. (2010). Depth profiles in a tropical, volcanic critical zone observatory: Basse-

Terre, Guadeloupe. In *Water-Rock Interaction - Proceedings of the 13th International Conference on Water-Rock Interaction, WRI-13* (pp. 245–248). Retrieved from https://pennstate.pure.elsevier.com/en/publications/depth-profiles-in-a-tropical-volcanic-critical-zone-observatory-b

Callahan, R. P., Riebe, C. S., Pasquet, S., Ferrier, K. L., Grana, D., Sklar, L. S., ... Holbrook, W. S. (2020). Subsurface Weathering Revealed in Hillslope-Integrated Porosity Distributions. *Geophysical Research Letters*, *47*(15), e2020GL088322. Retrieved from http://agupubs.onlinelibrary.wiley.com/doi/abs/10.1029/2020GL088322 (_eprint: https://onlinelibrary.wiley.com/doi/pdf/10.1029/2020GL088322) doi: 10.1029/2020GL088322

Carrière, S. D., Chalikakis, K., Ollivier, C., Heath, T., Mangin, M., Kempf, J., ... Lapègue, J. (2018, October). Sustainable groundwater resources exploration and management in a complex geological setting as part of a humanitarian project (Mahafaly Plateau, Madagascar). *Environmental Earth Sciences*, *77*(21), 734. Retrieved from https://doi.org/10.1007/s12665-018-7909-1 doi: 10.1007/s12665-018-7909-1

Chicot, D., Mendoza, J., Zaoui, A., Louis, G., Lepingle, V., Roudet, F., & Lesage, J. (2011, October). Mechanical properties of magnetite (Fe3O4), hematite (α-Fe2O3) and goethite (α-FeO·OH) by instrumented indentation and molecular dynamics analysis. *Materials Chemistry and Physics*, *129*(3), 862–870. Retrieved from http://www.sciencedirect.com/science/article/pii/S0254058411004627 doi: 10.1016/j.matchemphys.2011.05.056

Clergue, C., Dellinger, M., Buss, H. L., Gaillardet, J., Benedetti, M. F., & Dessert, C. (2015, October). Influence of atmospheric deposits and secondary minerals on Li isotopes budget in a highly weathered catchment, Guadeloupe (Lesser Antilles). *Chemical Geology*, *414*, 28–41. Retrieved from http://www.sciencedirect.com/science/article/pii/S0009254115300152 doi: 10.1016/j.chemgeo.2015.08.015

Comas, X., Wright, W., Hynek, S. A., Fletcher, R. C., & Brantley, S. L. (2019). Understanding fracture distribution and its relation to knickpoint evolution in the Rio Icacos watershed (Luquillo Critical Zone Observatory, Puerto Rico) using landscape-scale hydrogeophysics. *Earth Surface Processes and Landforms*, *44*(4), 877–885. Retrieved from http://onlinelibrary.wiley.com/doi/abs/10.1002/esp.4540 (_eprint: https://onlinelibrary.wiley.com/doi/pdf/10.1002/esp.4540) doi: 10.1002/esp.4540

de Marsily, G. (1986). *Quantitative Hydrogeology: Groundwater Hydrology for Engineers.* Academic Press.

Dessert, C., Clergue, C., Rousteau, A., Crispi, O., & Benedetti, M. F. (2020, January). Atmospheric contribution to cations cycling in highly weathered catchment, Guadeloupe (Lesser Antilles). *Chemical Geology*, *531*, 119354. Retrieved from http://www.sciencedirect.com/science/article/pii/S0009254119304838 doi: 10.1016/j.chemgeo.2019.119354

Dessert, C., Dupré, B., François, L. M., Schott, J., Gaillardet, J., Chakrapani, G., & Bajpai, S. (2001, June). Erosion of Deccan Traps determined by river geochemistry: impact on the global climate and the 87Sr/86Sr ratio of seawater. *Earth and Planetary Science Letters*, *188*(3), 459–474. Retrieved from https://www.sciencedirect.com/science/article/pii/S0012821X0100317X doi: 10.1016/S0012-821X(01)00317-X

Dessert, C., Lajeunesse, E., Lloret, E., Clergue, C., Crispi, O., Gorge, C., & Quidelleur, X. (2015, December). Controls on chemical weathering on a mountainous volcanic tropical island: Guadeloupe (French West Indies). *Geochimica et Cosmochimica Acta*, *171*, 216–237. Retrieved from http://www.sciencedirect.com/science/article/pii/S0016703715005384 doi: 10.1016/j.gca.2015.09.009

Eppinger, B. J., Hayes, J. L., Carr, B. J., Moon, S., Cosans, C. L., Holbrook, W. S., … Plante, Z. T. (2021). Quantifying Depth-Dependent Seismic Anisotropy in the Critical Zone Enhanced by Weathering of a Piedmont Schist. *Journal of Geophysical Research: Earth Surface*, *126*(10), e2021JF006289. Retrieved from http://onlinelibrary.wiley.com/doi/abs/10.1029/2021JF006289 (_eprint: https://agupubs.onlinelibrary.wiley.com/doi/pdf/10.1029/2021JF006289) doi: 10.1029/2021JF006289

Fan, Y., Li, H., & Miguez-Macho, G. (2013, February). Global Patterns of Groundwater Table Depth. *Science*, *339*(6122), 940–943. Retrieved from https://science-sciencemag-org.insu.bib.cnrs.fr/content/339/6122/940 (Publisher: American Association for the Advancement of Science Section: Report) doi: 10.1126/science.1229881

Flinchum, B. A., Banks, E., Hatch, M., Batelaan, O., Peeters, L. J. M., & Pasquet, S. (2020, September). Identifying recharge under subtle ephemeral features in a flat-lying semi-arid region using a combined geophysical approach. *Hydrology and Earth System Sciences*, *24*(9), 4353–4368. Retrieved from https://hess.copernicus.org/articles/24/4353/2020/ (Publisher: Copernicus GmbH) doi: https://doi.org/10.5194/hess-24-4353-2020

Flinchum, B. A., Holbrook, W. S., Grana, D., Parsekian, A. D., Carr, B. J., Hayes, J. L., & Jiao, J. (2018, October). Estimating the water holding capacity of the critical zone using near-surface geophysics. *Hydrological Processes*, *32*(22), 3308–3326. Retrieved from https://onlinelibrary.wiley.com/doi/abs/10.1002/hyp.13260 doi: 10.1002/hyp.13260

Flinchum, B. A., Holbrook, W. S., Parsekian, A. D., & Carr, B. J. (2019, August). Characterizing the Critical Zone Using Borehole and Surface Nuclear Magnetic Resonance. *Vadose Zone Journal*, *18*(1). Retrieved from https://dl.sciencesocieties.org/publications/vzj/abstracts/18/1/180209 doi: 10.2136/vzj2018.12.0209

Flinchum, B. A., Holbrook, W. S., Rempe, D., Moon, S., Riebe, C. S., Carr, B. J., … Peters, M. P. (2018). Critical Zone Structure Under a Granite Ridge Inferred From Drilling and Three-Dimensional Seismic Refraction Data. *Journal of Geophysical Research: Earth Surface*, *123*(6), 1317–1343. Retrieved from http://agupubs.onlinelibrary.wiley.com/doi/abs/10.1029/2017JF004280 doi: 10.1029/2017JF004280

Floury, P., Gaillardet, J., Tallec, G., Ansart, P., Bouchez, J., Louvat, P., & Gorge, C. (2019). Chemical weathering and CO2 consumption rate in a multilayered-aquifer dominated watershed under intensive farming: The Orgeval Critical Zone Observatory, France. *Hydrological Processes*, *33*(2), 195–213. Retrieved from https://onlinelibrary.wiley.com/doi/abs/10.1002/hyp.13340 doi: 10.1002/hyp.13340

Gaillardet, J., Braud, I., Hankard, F., Anquetin, S., Bour, O., Dorfliger, N., … Zitouna, R. (2018, November). OZCAR: The French Network of Critical Zone Observatories. *Vadose Zone Journal*, *17*(1). Retrieved from https://dl.sciencesocieties.org/publications/vzj/abstracts/17/1/180067 doi: 10.2136/vzj2018.04.0067

Gaillardet, J., Rad, S., Rivé, K., Louvat, P., Gorge, C., Allègre, C. J., & Lajeunesse, E. (2011, December). Orography-driven chemical denudation in the Lesser Antilles: Evidence for a new feed-back mechanism stabilizing atmospheric CO2. *American Journal of Science*, *311*(10), 851–894. Retrieved from https://www.ajsonline.org/content/311/10/851 (Publisher: American Journal of Science Section: Articles) doi: 10.2475/10.2011.02

Gase, A., Bradford, J., & Brand, B. (2018, January). Estimation of porosity and water saturation in dual-porosity pyroclastic deposits from joint analysis of compression, shear, and electromagnetic velocities. *Geophysics*, ID1–ID11. Retrieved from https://library.seg.org/doi/abs/10.1190/geo2017-0234.1 doi: 10.1190/geo2017-0234.1

Glover, P. W. J. (2010, November). A generalized Archie's law for n phases. *GEOPHYSICS*, *75*(6), E247–E265. Retrieved from https://library.seg.org/doi/full/10.1190/1.3509781 (Publisher: Society of Exploration Geophysicists) doi: 10.1190/1.3509781

Graham, R., Rossi, A., & Hubbert, R. (2010, February). Rock to regolith conversion: Producing hospitable substrates for terrestrial ecosystems. *GSA Today*, 4–9. Retrieved from http://www.geosociety.org/gsatoday/archive/20/2/abstract/i1052-5173-20-2-4.htm doi: 10.1130/GSAT57A.1

Grelle, G., & Guadagno, F. M. (2009, July). Seismic refraction methodology for groundwater level determination: "Water seismic index". *Journal of Applied Geophysics*, *68*(3), 301–320. Retrieved from http://www.sciencedirect.com/science/article/pii/S0926985109000202 doi: 10.1016/j.jappgeo.2009.02.001

Gu, X., Heaney, P. J., Reis, F. D. A. A., & Brantley, S. L. (2020, October). Deep abiotic weathering of pyrite. *Science*, *370*(6515). Retrieved from http://science.sciencemag.org/content/370/6515/eabb8092 (Publisher: American Association for the Advancement of Science Section: Research Article) doi: 10.1126/science.abb8092

Gu, X., Rempe, D. M., Dietrich, W. E., West, A. J., Lin, T.-C., Jin, L., & Brantley, S. L. (2020, January). Chemical reactions, porosity, and microfracturing in shale during weathering: The effect of erosion rate. *Geochimica et Cosmochimica Acta*, *269*, 63–100. Retrieved from https://www.sciencedirect.com/science/article/pii/S0016703719306386 doi: 10.1016/j.gca.2019.09.044

Guérin, A., Devauchelle, O., Robert, V., Kitou, T., Dessert, C., Quiquerez, A., … Lajeunesse, E. (2019). Stream-Discharge Surges Generated by Groundwater Flow. *Geophysical Research Letters*, *46*(13), 7447–7455. Retrieved from http://agupubs.onlinelibrary.wiley.com/doi/abs/10.1029/2019GL082291 doi: 10.1029/2019GL082291

Haitjema, H. M., & Mitchell-Bruker, S. (2005). Are Water Tables a Subdued Replica of the Topography? *Groundwater*, *43*(6), 781–786. doi: 10.1111/j.1745-6584.2005.00090.x

Harman, C. J., & Cosans, C. L. (2019). A low-dimensional model of bedrock weathering and lateral flow coevolution in hillslopes: 2. Controls on weathering and permeability profiles, drainage hydraulics, and solute export pathways. *Hydrological Processes*, *33*(8), 1168–1190. Retrieved from http://onlinelibrary.wiley.com/doi/abs/10.1002/hyp.13385 doi: 10.1002/hyp.13385

Hayes, J. L., Riebe, C. S., Holbrook, W. S., Flinchum, B. A., & Hartsough, P. C. (2019, September). Porosity production in weathered rock: Where volumetric strain dominates over chemical mass loss. *Science Advances*, *5*(9), eaao0834. Retrieved from https://advances.sciencemag.org/content/5/9/eaao0834 doi: 10.1126/sciadv.aao0834

Heap, M. J., Baumann, T. S., Rosas-Carbajal, M., Komorowski, J.-C., Gilg, H. A., Villeneuve, M., … Reuschlé, T. (2021). Alteration-Induced Volcano Instability at La Soufrière de Guadeloupe (Eastern Caribbean). *Journal of Geophysical Research: Solid Earth*, *126*(8), e2021JB022514. Retrieved from http://onlinelibrary.wiley.com/doi/abs/10.1029/2021JB022514 (_eprint: https://agupubs.onlinelibrary.wiley.com/doi/pdf/10.1029/2021JB022514) doi: 10.1029/2021JB022514

Hector, B., Séguis, L., Hinderer, J., Cohard, J.-M., Wubda, M., Descloitres, M., … Boy, J.-P. (2015, October). Water storage changes as a marker for base flow generation processes in a tropical humid basement catchment (Benin): Insights from hybrid gravimetry. *Water Resources Research*, *51*(10), 8331–8361. Retrieved from https://agupubs.onlinelibrary.wiley.com/doi/full/10.1002/2014WR015773 doi: 10.1002/2014WR015773

Holbrook, W. S., Marcon, V., Bacon, A. R., Brantley, S. L., Carr, B. J., Flinchum, B. A., ... Riebe, C. S. (2019, March). Links between physical and chemical weathering inferred from a 65-m-deep borehole through Earth's critical zone. *Scientific Reports*, *9*(1), 4495. Retrieved from https://www.nature.com/articles/s41598-019-40819-9 doi: 10.1038/s41598-019-40819-9

Holbrook, W. S., Riebe, C. S., Elwaseif, M., L. Hayes, J., Basler-Reeder, K., L. Harry, D., ... W. Hopmans, J. (2014, March). Geophysical constraints on deep weathering and water storage potential in the Southern Sierra Critical Zone Observatory. *Earth Surface Processes and Landforms*, *39*(3), 366–380. Retrieved from http://onlinelibrary.wiley.com/doi/10.1002/esp.3502/abstract doi: 10.1002/esp.3502

Hubbard, S. S., & Linde, N. (2011). Hydrogeophysics. In *Treatise on Water Science* (pp. 401–434). Elsevier. Retrieved from http://www.sciencedirect.com/science/article/pii/B9780444531995000439

Jeanneau, L., Buysse, P., Denis, M., Gruau, G., Petitjean, P., Jaffrézic, A., ... Viaud, V. (2020, March). Water Table Dynamics Control Carbon Losses from the Destabilization of Soil Organic Matter in a Small, Lowland Agricultural Catchment. *Soil Systems*, *4*(1), 2. Retrieved from https://www.mdpi.com/2571-8789/4/1/2 (Number: 1 Publisher: Multidisciplinary Digital Publishing Institute) doi: 10.3390/soilsystems4010002

Jougnot, D., Ghorbani, A., Revil, A., Leroy, P., & Cosenza, P. (2010, January). Spectral induced polarization of partially saturated clay-rocks: a mechanistic approach. *Geophysical Journal International*, *180*(1), 210–224. Retrieved from https://doi.org/10.1111/j.1365-246X.2009.04426.x doi: 10.1111/j.1365-246X.2009.04426.x

Kolbe, T., Marçais, J., Dreuzy, J.-R. d., Labasque, T., & Bishop, K. (2020). Lagged rejuvenation of groundwater indicates internal flow structures and hydrological connectivity. *Hydrological Processes*, *34*(10), 2176–2189. Retrieved from https://onlinelibrary.wiley.com/doi/abs/10.1002/hyp.13753 (_eprint: https://onlinelibrary.wiley.com/doi/pdf/10.1002/hyp.13753) doi: 10.1002/hyp.13753

Lana-Renault, N., Latron, J., & Regüés, D. (2007, December). Streamflow response and water-table dynamics in a sub-Mediterranean research catchment (Central Pyrenees). *Journal of Hydrology*, *347*(3), 497–507. Retrieved from http://www.sciencedirect.com/science/article/pii/S0022169407005380 doi: 10.1016/j.jhydrol.2007.09.037

Lebedeva, M. I., & Brantley, S. L. (2020). Relating the depth of the water table to the depth of weathering. *Earth Surface Processes and Landforms*, *45*(9), 2167–2178. Retrieved from https://onlinelibrary.wiley.com/doi/abs/10.1002/esp.4873 (_eprint: https://onlinelibrary.wiley.com/doi/pdf/10.1002/esp.4873) doi: 10.1002/esp.4873

Linde, N., Revil, A., Bolève, A., Dagès, C., Castermant, J., Suski, B., & Voltz, M. (2007, February). Estimation of the water table throughout a catchment using self-potential and piezometric data in a Bayesian framework. *Journal of Hydrology*, *334*(1), 88–98. Retrieved from http://www.sciencedirect.com/science/article/pii/S0022169406005142 doi: 10.1016/j.jhydrol.2006.09.027

Louvat, P., & Allègre, C. J. (1997, September). Present denudation rates on the island of Réunion determined by river geochemistry: Basalt weathering and mass budget between chemical and mechanical erosions. *Geochimica et Cosmochimica Acta*, *61*(17), 3645–3669. Retrieved from https://

www.sciencedirect.com/science/article/pii/S0016703797001804 doi: 10.1016/S0016-7037(97)00180-4

Mahindawansha, A., Orlowski, N., Kraft, P., Rothfuss, Y., Racela, H., & Breuer, L. (2018, August). Quantification of plant water uptake by water stable isotopes in rice paddy systems. *Plant and Soil*, *429*(1), 281–302. Retrieved from https://doi.org/10.1007/s11104-018-3693-7 doi: 10.1007/s11104-018-3693-7

Maillot, M., Flipo, N., Rivière, A., Desassis, N., Renard, D., Goblet, P., & Vincent, M. (2019, November). Technical note: Water table mapping accounting for river–aquifer connectivity and human pressure. *Hydrology and Earth System Sciences*, *23*(11), 4835–4849. Retrieved from https://hess.copernicus.org/articles/23/4835/2019/ (Publisher: Copernicus GmbH) doi: 10.5194/hess-23-4835-2019

Mindlin, R. D. (1949). Compliance of elastic bodies in contact. *Journal of Applied Mechanics*, *16*, 259–268.

Müller, S., & Schüler, L. (2021, July). *GeoStat-Framework/GSTools: v1.3.2 'Pure Pink'.* Zenodo. Retrieved from https://zenodo.org/record/5068979 (Language: eng) doi: 10.5281/zenodo.5068979

Neducza, B. (2007). Stacking of surface waves. *Geophysics*, *72*(2), 51–58. Retrieved from http://link.aip.org/link/?GPY/72/V51/1 doi: 10.1190/1.2431635

Nevers, P., Bouchez, J., Gaillardet, J., Thomazo, C., Charpentier, D., Faure, L., & Bertrand, C. (2021, June). Landslides as geological hotspots of CO_2 emission: clues from the instrumented Séchilienne landslide, western European Alps. *Earth Surface Dynamics*, *9*(3), 487–504. Retrieved from https://esurf.copernicus.org/articles/9/487/2021/ (Publisher: Copernicus GmbH) doi: 10.5194/esurf-9-487-2021

Novitsky, C. G., Holbrook, W. S., Carr, B. J., Pasquet, S., Okaya, D., & Flinchum, B. A. (2018, January). Mapping inherited fractures in the Critical Zone using seismic anisotropy from circular surveys. *Geophysical Research Letters*, *45*(7), 3126–3135. Retrieved from http://agupubs.onlinelibrary.wiley.com/doi/abs/10.1002/2017GL075976 doi: 10.1002/2017GL075976

NRC. (2001). *Basic research opportunities in Earth Science.* Washington DC: The National Academies Press. Retrieved from https://www.nap.edu/catalog/9981/basic-research-opportunities-in-earth-science doi: 10.17226/9981

Olona, J., Pulgar, J., Fernández-Viejo, G., López-Fernández, C., & González-Cortina, J. (2010, December). Weathering variations in a granitic massif and related geotechnical properties through seismic and electrical resistivity methods. *Near Surface Geophysics*, *8*(6), 585–599. Retrieved from http://www.earthdoc.org/detail.php?pubid=43265 doi: 10.3997/1873-0604.2010043

O'Neill, A., Dentith, M., & List, R. (2003, January). Full-waveform P-SV reflectivity inversion of surface waves for shallow engineering applications. *Exploration Geophysics*, *34*(3), 158–173. Retrieved from http://www.publish.csiro.au/paper/EG03158

Orlando, J., Comas, X., Hynek, S. A., Buss, H. L., & Brantley, S. L. (2016). Architecture of the deep critical zone in the Río Icacos watershed (Luquillo Critical Zone Observatory, Puerto Rico) inferred from drilling and ground penetrating radar (GPR). *Earth Surface Processes and Landforms*, *41*(13), 1826–1840. Retrieved from http://onlinelibrary.wiley.com/doi/abs/10.1002/esp.3948 (_eprint: https://onlinelibrary.wiley.com/doi/pdf/10.1002/esp.3948) doi: 10.1002/esp.3948

Parsekian, A. D., Grana, D., Neves, F. d. A., Pleasants, M. S., Seyfried, M., Moravec, B. G., … Kelleners, T. (2021, February). Hydrogeophysical comparison of hillslope critical zone architecture for different geologic substrates.

Geophysics, 1–84. Retrieved from https://library.seg.org/doi/abs/10.1190/geo2020-0438.1 (Publisher: Society of Exploration Geophysicists) doi: 10.1190/geo2020-0438.1

Parsekian, A. D., Singha, K., Minsley, B. J., Holbrook, W. S., & Slater, L. (2015, March). Multiscale geophysical imaging of the critical zone. *Reviews of Geophysics*, *53*(1), 2014RG000465. Retrieved from http://onlinelibrary.wiley.com/doi/10.1002/2014RG000465/abstract doi: 10.1002/2014RG000465

Pasquet, S., & Bodet, L. (2017, July). SWIP: An integrated workflow for surface-wave dispersion inversion and profiling. *Geophysics*, *82*(6), WB47–WB61. Retrieved from http://library.seg.org/doi/abs/10.1190/geo2016-0625.1 doi: 10.1190/geo2016-0625.1

Pasquet, S., Bodet, L., Dhemaied, A., Mouhri, A., Vitale, Q., Rejiba, F., … Guérin, R. (2015, February). Detecting different water table levels in a shallow aquifer with combined P-, surface and SH-wave surveys: Insights from VP/VS or Poisson's ratios. *Journal of Applied Geophysics*, *113*, 38–50. Retrieved from http://www.sciencedirect.com/science/article/pii/S0926985114003589 doi: 10.1016/j.jappgeo.2014.12.005

Pasquet, S., Bodet, L., Longuevergne, L., Dhemaied, A., Camerlynck, C., Rejiba, F., & Guérin, R. (2015, August). 2D characterization of near-surface VP/VS: surface-wave dispersion inversion versus refraction tomography. *Near Surface Geophysics*, *13*(4), 315–331. Retrieved from http://nsg.eage.org/publication/publicationdetails/?publication=81945 doi: 10.3997/1873-0604.2015028

Pasquet, S., Holbrook, W. S., Carr, B. J., & Sims, K. W. W. (2016, December). Geophysical imaging of shallow degassing in a Yellowstone hydrothermal system. *Geophysical Research Letters*, *43*(23), 2016GL071306. Retrieved from http://onlinelibrary.wiley.com/doi/10.1002/2016GL071306/abstract doi: 10.1002/2016GL071306

Pasquet, S., Wang, W., Chen, P., & Flinchum, B. A. (2020, December). Multiwindow weighted stacking of surface-wave dispersion. *Geophysics*, *86*(2), EN39–EN50. Retrieved from https://library.seg.org/doi/full/10.1190/geo2020-0096.1 (Publisher: Society of Exploration Geophysicists) doi: 10.1190/geo2020-0096.1

Pride, S. R. (2005, January). Relationships between seismic and hydrological properties. In *Hydrogeophysics* (pp. 253–290). Springer. Retrieved from http://link.springer.com/chapter/10.1007/1-4020-3102-5_9

Rempe, D. M., & Dietrich, W. E. (2014, May). A bottom-up control on fresh-bedrock topography under landscapes. *Proceedings of the National Academy of Sciences*, *111*(18), 6576–6581. Retrieved from https://www.pnas.org/content/111/18/6576 doi: 10.1073/pnas.1404763111

Rempe, D. M., & Dietrich, W. E. (2018, March). Direct observations of rock moisture, a hidden component of the hydrologic cycle. *Proceedings of the National Academy of Sciences*, *115*(11), 2664–2669. Retrieved from https://www.pnas.org/content/115/11/2664 doi: 10.1073/pnas.1800141115

Riebe, C. S., Hahm, W. J., & Brantley, S. L. (2017, January). Controls on deep critical zone architecture: a historical review and four testable hypotheses. *Earth Surface Processes and Landforms*, *42*(1), 128–156. Retrieved from http://onlinelibrary.wiley.com/doi/10.1002/esp.4052/abstract doi: 10.1002/esp.4052

Rücker, C., Günther, T., & Wagner, F. M. (2017, December). pyGIMLi: An open-source library for modelling and inversion in geophysics. *Computers & Geosciences*, *109*, 106–123. Retrieved from http://www.sciencedirect.com/science/article/pii/S0098300417300584 doi: 10.1016/j.cageo.2017.07.011

Sak, P. B., Miller, S. R., Ma, L., & Gaillardet, J. (2018, November). Fluvial knickpoints and transient erosion on Basse-Terre, Guadeloupe, with implications for estimates of chemical weathering. Indianapolis IN, USA: GSA. Retrieved from https://gsa.confex.com/gsa/2018AM/webprogram/Paper324209.html

Santamarina, J. C., Rinaldi, V. A., Fratta, D., Klein, K. A., Wang, Y.-H., Cho, G. C., & Cascante, G. (2005, January). A survey of elastic and electromagnetic properties of near-surface soils. In *Near-Surface Geophysics* (pp. 71–88). Society of Exploration Geophysicists. Retrieved from http://library.seg.org/doi/abs/10.1190/1.9781560801719.ch4

Shi, P., Huang, Y., Ji, W., Xiang, W., Evaristo, J., & Li, Z. (2021, April). Impacts of deep-rooted fruit trees on recharge of deep soil water using stable and radioactive isotopes. *Agricultural and Forest Meteorology*, *300*, 108325. Retrieved from http://www.sciencedirect.com/science/article/pii/S0168192321000083 doi: 10.1016/j.agrformet.2021.108325

Snyder, D. T. (2008). Estimated Depth to Ground Water and Configuration of the Water Table in the Portland, Oregon Area. doi: 10.3133/SIR20085059

St. Clair, J., Moon, S., Holbrook, W. S., Perron, J. T., Riebe, C. S., Martel, S. J., ... Richter, D. d. (2015, October). Geophysical imaging reveals topographic stress control of bedrock weathering. *Science*, *350*(6260), 534–538. Retrieved from http://www.sciencemag.org/content/350/6260/534 doi: 10.1126/science.aab2210

Stumpp, C., & Hose, G. C. (2013, November). The impact of water table drawdown and drying on subterranean aquatic fauna in in-vitro experiments. *PLoS ONE*, *8*(11), e78502. Retrieved from http://dx.doi.org/10.1371/journal.pone.0078502 doi: 10.1371/journal.pone.0078502

Tromp-van Meerveld, H. J., & McDonnell, J. J. (2006). Threshold Relations in Subsurface Stormflow: 1. A 147-Storm Analysis of the Panola Hillslope. *Water Resources Research*, *42*(2), W02410. doi: 10.1029/2004WR003778

Turkeltaub, T., Ascott, M. J., Gooddy, D. C., Jia, X., Shao, M.-A., & Binley, A. (2020). Prediction of regional-scale groundwater recharge and nitrate storage in the vadose zone: A comparison between a global model and a regional model. *Hydrological Processes*, *34*(15), 3347–3357. Retrieved from http://onlinelibrary.wiley.com/doi/abs/10.1002/hyp.13834 (_eprint: https://onlinelibrary.wiley.com/doi/pdf/10.1002/hyp.13834) doi: 10.1002/hyp.13834

Wang, W., Chen, P., Dueker, K., Zhang, Y., Lee, E.-j., Mu, D., ... Jiao, J. (2021). Coevolution of Weathering Front and Water Table. *Geophysical Research Letters*, *48*(20), e2021GL092916. Retrieved from http://onlinelibrary.wiley.com/doi/abs/10.1029/2021GL092916 (_eprint: https://agupubs.onlinelibrary.wiley.com/doi/pdf/10.1029/2021GL092916) doi: 10.1029/2021GL092916

Wang, W., Nyblade, A., Mount, G., Moon, S., Chen, P., Accardo, N., ... Brantley, S. L. (2022). 3D seismic anatomy of a watershed reveals climate-topography coupling that drives water flowpaths and bedrock weathering. *Journal of Geophysical Research: Earth Surface*, *n/a*(n/a), e2021JF006281. Retrieved from http://onlinelibrary.wiley.com/doi/abs/10.1029/2021JF006281 (_eprint: https://agupubs.onlinelibrary.wiley.com/doi/pdf/10.1029/2021JF006281) doi: 10.1029/2021JF006281

Wathelet, M., Jongmans, D., & Ohrnberger, M. (2004, November). Surface-wave inversion using a direct search algorithm and its application to ambient vibration measurements. *Near Surface Geophysics*, *2*(4), 211–221. Retrieved from http://earthdoc.eage.org/detail.php?pubid=8129 doi: 10.3997/1873-0604.2004018

Waxman, M., & Smits, L. (1968, June). Electrical Conductivities in Oil-Bearing Shaly Sands. *Society of Petroleum Engineers Journal*, *8*(02), 107–122. Retrieved from `https://doi.org/10.2118/1863-A` doi: 10.2118/1863-A

Weiler, M., McDonnell, J. J., Tromp-van Meerveld, I., & Uchida, T. (2006). Subsurface Stormflow. In *Encyclopedia of Hydrological Sciences.* John Wiley & Sons, Ltd. Retrieved from `http://onlinelibrary.wiley.com/doi/10.1002/0470848944.hsa119/abstract`

White, A. F., Blum, A. E., Schulz, M. S., Vivit, D. V., Stonestrom, D. A., Larsen, M., ... Eberl, D. (1998). Chemical Weathering in a Tropical Watershed, Luquillo Mountains, Puerto Rico: I. Long-Term Versus Short-Term Weathering Fluxes. *Geochimica et Cosmochimica Acta*, *62*(2), 209–226. doi: 10.1016/S0016-7037(97)00335-9

Wilford, J., & Thomas, M. (2013, September). Predicting regolith thickness in the complex weathering setting of the central Mt Lofty Ranges, South Australia. *Geoderma*, *206*, 1–13. Retrieved 2019-12-18, from `http://www.sciencedirect.com/science/article/pii/S0016706113001122` doi: 10.1016/j.geoderma.2013.04.002

Yaede, J. R., McBride, J. H., Nelson, S. T., Park, C. B., Flores, J. A., Turnbull, S. J., ... Gardner, N. L. (2015, April). A geophysical strategy for measuring the thickness of the critical zone developed over basalt lavas. *Geosphere*, *11*(2), 514–532. Retrieved from `http://pubs.geoscienceworld.org/geosphere/article/11/2/514/132242/A-geophysical-strategy-for-measuring-the-thickness` doi: 10.1130/GES01142.1

Figure 1.

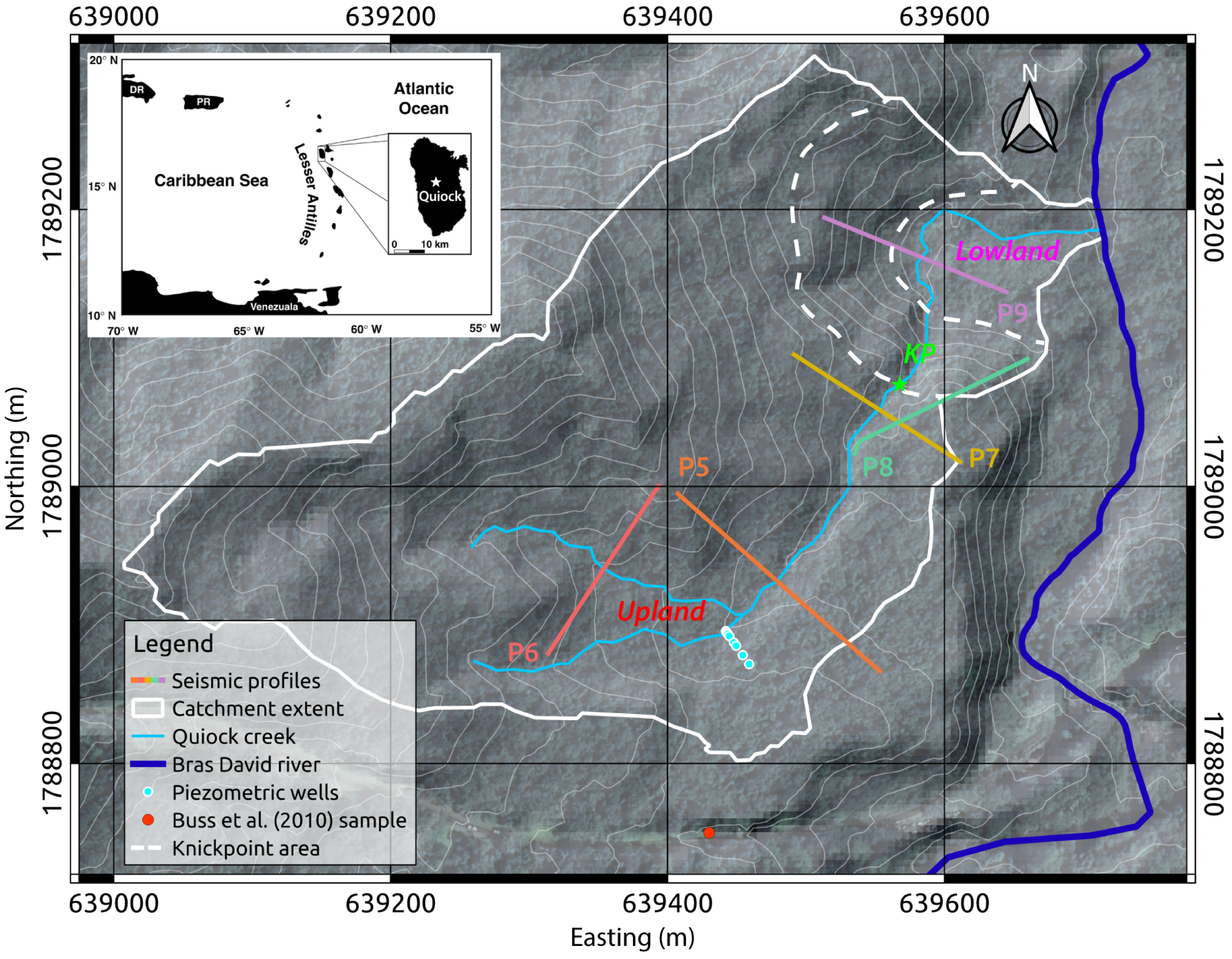

639000
639200
639400
639600
Northing (m)
1789200
1789000
1788800
Easting (m)
20° N
15° N
10° N
70° W
65° W
60° W
55° W
DR
PR
Atlantic Ocean
Caribbean Sea
Lesser Antilles
Venezuala
Quiock
0
10 km
N
Lowland
P9
KP
P7
P8
P5
Upland
P6
Legend
Seismic profiles
Catchment extent
Quiock creek
Bras David river
Piezometric wells
Buss et al. (2010) sample
Knickpoint area

Figure 2.

a.
Northing (m)
Elevation (m)
Easting (m)
Upland
Knickpoint
Lowland
Bras David river
Quiock creek
P5
P6
P7
P8
P9
N
b.
c.
d.
e.
f.
g.
h.
i.
j.
k.
Distance (m)
Elevation (m)
Vp (m/s)
Water saturation W

Figure 3.

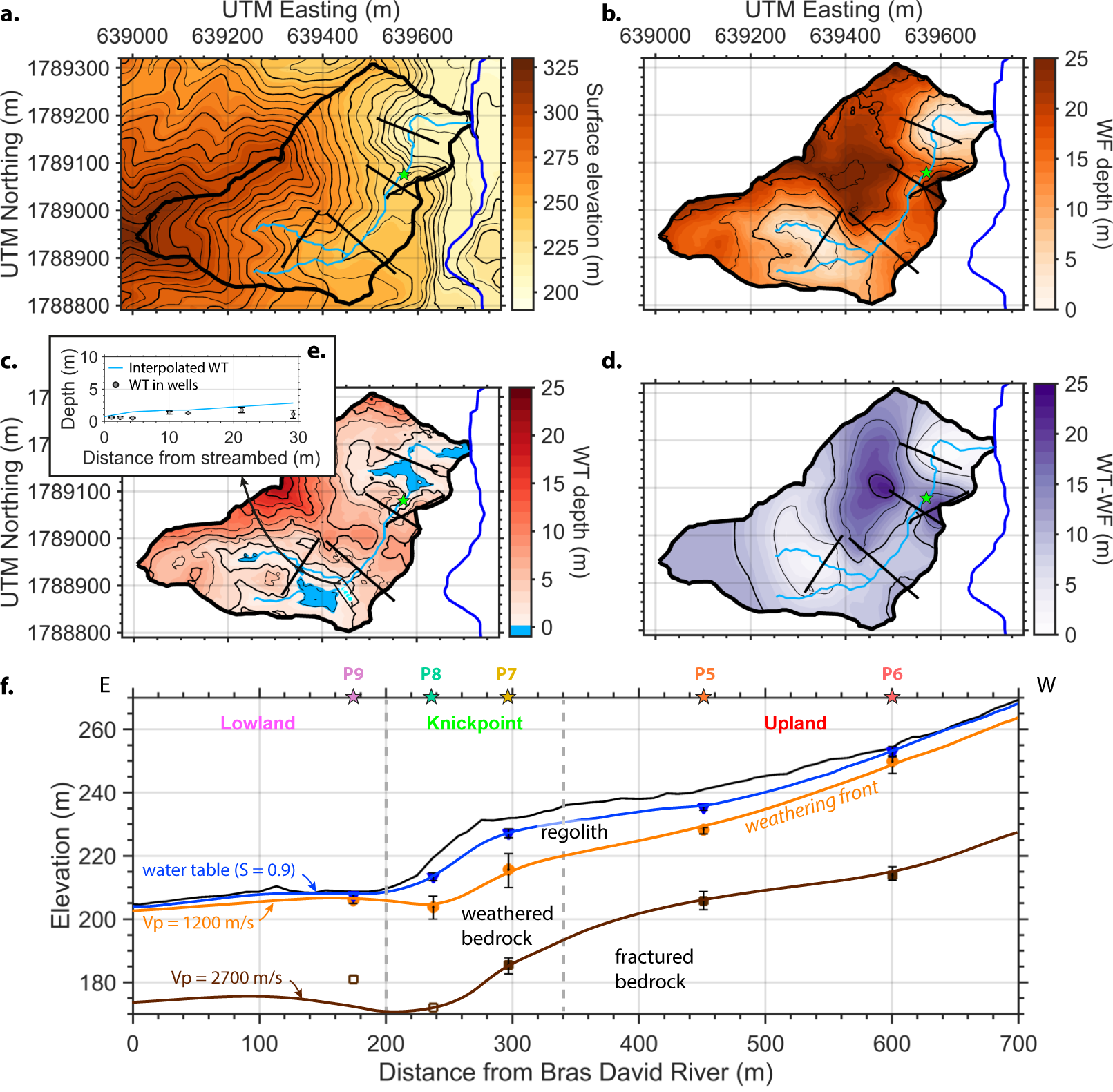
a.
UTM Easting (m)
UTM Northing (m)
Surface elevation (m)
b.
WF depth (m)
c.
WT depth (m)
d.
WT-WF (m)
e.
Interpolated WT
WT in wells
Depth (m)
Distance from streambed (m)
f.
E
W
P9
P8
P7
P5
P6
Lowland
Knickpoint
Upland
regolith
weathering front
water table (S = 0.9)
Vp = 1200 m/s
weathered bedrock
fractured bedrock
Vp = 2700 m/s
Elevation (m)
Distance from Bras David River (m)

Supporting Information for "Geophysical imaging of the deep critical zone architecture reveals the complex interplay between hydrological and weathering processes in a volcanic tropical catchment"

S. Pasquet[1], J. Marçais[2], J. L. Hayes[3], P. Sak[3,4], L. Ma[5] and J. Gaillardet[1]

[1]Université de Paris, Institut de physique du globe de Paris, CNRS, Paris, France

[2]INRAE, UR RiverLy, Villeurbanne, France

[3]Department of Earth Sciences, Dickinson College, Carlisle PA, USA

[4]Earth and Environmental Systems Institute and Department of Geosciences, Pennsylvania State University, University Park, PA, USA

[5]University of Texas at El Paso, El Paso TX, USA

Contents of this file

Introduction

Here we provide additional figures aimed at validating the processing, inversion and interpolation steps described in the main manuscript. We specifically give more details about the seismic acquisition, the SRT and MASW workflows, and give a complete description of the petrophysical model and its calibration procedure. We finally describe the average kriging procedure used to interpolate weathering front and water table depths.

S1. Seismic Data Acquisition

For both acquisition campaigns, we used 14-Hz vertical-component geophones, spaced at 4 m in 2016, and at 2 m in 2019. Shots were recorded every 10 m with a 5.4-kg sledgehammer swung onto a hard plate. For each shot, the sampling rate was 0.125 ms and the recording time was 850 ms in order to include the full seismic wavefield. Start and end points of each profile were recorded with a handheld GPS and relative elevations at each geophone location were measured using a laser rangefinder.

S2. Seismic Refraction Tomography

Tomographic inversions are performed in pyGIMLi (Rücker et al., 2017), where the inversion domain is parameterized with a 2D mesh of constant velocity tetrahedrons. Rays are traced through the mesh using a shortest path algorithm (Dijkstra, 1959; Moser, 1991) and updates are found by solving a regularized, linear inverse problem. We used 144 combinations of starting models and regularization parameters (Table S1) in order to explore the non-uniqueness of the inversion and estimate the uncertainty of the velocity distribution along each profile. A selection is then applied to keep only the inversions performed with a set of parameters that obtained a root mean square error < 2.5 ms and a $\chi^2 < 2$ for all the profiles. The selected models are then merged to create an average velocity model and its associated uncertainty. Models are masked at depth below the lowest raypath (Figure S1). The standard deviations along each profile are computed to estimate how the velocity likelihood varies laterally and at depth (Figure S2).

S3. Multichannel Analysis of Surface-wave

The seismic data were processed to perform surface-wave dispersion inversion and profiling (Pasquet & Bodet, 2017) using the SWIP software package (available at `https://github.com/SWIPdev/SWIP/releases`). SWIP uses windowing and stacking techniques (Neducza, 2007; O'Neill et al., 2003) to take advantage of redundant seismic data and retrieve a 2D model of V_S from a succession of 1D inversions. Dispersion images were extracted every 2 m along each profile with the novel multiwindow weighted stacking of surface-wave procedure (Pasquet et al., 2020), using a set of 6 windows with evenly spaced apertures ranging between 14 m and 94 m. For each window along the profile, dispersion images were computed for each aperture using all shots located between 4 and 20 m away from the windowed data subset. All 6 individual dispersion images were then stacked as one final image with increased signal to noise ratio, doing so every 2 m along the seismic profile. Dispersion curves are eventually identified and picked on each of the stacked images to characterize the lateral variability of the phase velocity *vs* frequency relationship.

Dispersion curves are then inverted with the neighborhood algorithm (NA) developed in (Sambridge, 1999) and implemented for subsurface applications within the open software package Geopsy (Wathelet et al., 2004). The NA carries out a random search within a pre-defined parameter space, i.e. V_P, V_S, density and thickness of each layer. In Geopsy, theoretical dispersion curves are computed from the elastic parameters using the Thomson-Haskell matrix propagator technique (Haskell, 1953; Thomson, 1950) as implemented in (Dunkin, 1965). We set the inversion parameterization as a stack of ten layers overlaying a half-space in order to correctly describe smooth velocity gradients encountered in such weathered materials. The thickness of each layer was set to be bound between 0.5 and 1.5 m in the upper layer, these limits then exponentially increasing in the following layers until reaching 1.5 and 6 m in the deepest layer. The valid parameter range for sampling velocity models was 10 to 2500 m/s for V_S, with velocities constrained to only increase with depth, while V_P was automatically parameterized from SRT results.

For each 1D inversion, models matching the observed data within the error bars are selected to build a misfit-weighted final model. After checking phase velocity residuals (Figure S3), the depth of investigation (DOI) is estimated from the standard deviation of all selected models, using a threshold of 15% on the standard deviation to determine the DOI and limit the extent of the V_S model (Figure S4). Each 1D V_S model is finally represented at its corresponding extraction position to create a 2D V_S section. We eventually compared observed and calculated phase velocity for each window position, and computed their residuals to check the quality of the inversion.

S4. Petrophysical inversion

In order to estimate porosity and saturation from V_P and V_S, we used a petrophysical model based on the Hertz-Mindlin contact theory. We followed the strategy presented by (Pasquet et al., 2016) and applied in an hydrothermal system in Yellowstone. The model is used to calculate bulk elastic parameters of the medium so as to simulate realistic values of V_P and V_S that can be compared to those measured with SRT and MASW. With this model, we represent the medium as an aggregate of randomly packed spheres and simulate their bulk elastic properties (i.e. bulk and shear modulus) as functions of the elastic properties of constituent minerals, porosity, saturation, and several model parameters.

We assumed a unique mineralogical composition in the grain following the description by Buss et al. (2010) (66% clay, 28% hydroxides and 6% quartz). For each mineral compound, we use the elastic parameters found in the literature and summarized in Table S2. The elastic parameters (K_g and G_g) of the grains are then computed from this mineralogical composition with the Voigt-Reuss-Hill average (Hill, 1952; Mavko et al., 2003):

$$(K_g, G_g) = \frac{1}{2}\left[\sum_{i=1}^{m} f_i(K_i, G_i) + \left(\sum_{i=1}^{m} \frac{f_i}{(K_i, G_i)}\right)^{-1}\right], \tag{1}$$

where m is the number of mineral constituents, f_i is the volumetric fraction of the i-th constituent of the solid phase, and K_i and G_i are the bulk and shear moduli of the i-th constituent, respectively. From K_g and G_g, we can compute the Poisson's ratio ν_g of the grains:

$$\nu_g = \frac{1}{2}\left(\frac{3K_g - 2G_g}{3K_g + G_g}\right), \tag{2}$$

while their density ρ_g is calculated following:

$$\rho_g = \sum_{i=1}^{m} f_i \rho_i. \tag{3}$$

The bulk density of the medium (ρ_b) can then be calculated for different combinations of porosity (Φ) and saturation (W) with the following equation:

$$\rho_b = \Phi(W\rho_w + (1 - W)\rho_a) + (1 - \Phi)\rho_g, \tag{4}$$

where ρ_w and ρ_a are the densities of water and air, respectively.

At this point we can compute the bulk elastic parameters of the dry rock frame made of a random pack of identical spherical grains subject to a hydrostatic pressure P_{eff}. The bulk modulus K_{HM} is computed as follow:

$$K_{HM} = \left[\frac{n^2(1 - \Phi_c)^2 G_g^2}{18\pi^2(1 - \nu_g)^2} P_{eff}\right]^{\frac{1}{3}}, \tag{5}$$

where n is the average number of contacts between grains and Φ_c a critical porosity over which the medium changes from a suspension to a grain-supported material. As recommended by Nur, Mavko, Dvorkin, and Galmudi (1998), we used a critical porosity of 0.36. Since the traditional Hertz-Mindlin formulation tends to overestimate shear-wave velocities in unconsolidated media (Bachrach & Avseth, 2008), we use the approach proposed by Mavko et al. (2003) to calculate the shear modulus (G_{HM}). This approach allows a fraction f of the grain contacts to be frictionless, the rest having perfect adhesion:

$$G_{HM} = \frac{2 + 3f - (1 + 3f)\nu_g}{5(2 - \nu_g)} \left[\frac{3n^2(1 - \Phi_c)^2 G_g^2}{2\pi^2(1 - \nu_g)^2} P_{eff}\right]^{\frac{1}{3}}, \tag{6}$$

In the case of full saturation, P_{eff} is calculated as follow:

$$P_{eff} = (\rho_b - \rho_w) g D, \tag{7}$$

where g is the gravitational acceleration and D is the depth below ground level. In partially saturated media, P_{eff} is calculated as:

$$P_{eff} = \rho_b g D. \tag{8}$$

For porosity Φ higher than Φ_c, the effective bulk (K_{dry}) and shear (G_{dry}) moduli of the dry frame are calculated with the modified upper Hashin-Shtrikman (H-S) bound (Dvorkin et al., 1999):

$$K_{dry} = \left[\frac{\frac{1-\Phi}{1-\Phi_c}}{K_{HM} + \frac{4}{3}G_{HM}} + \frac{\frac{\Phi-\Phi_c}{1-\Phi_c}}{\frac{4}{3}G_{HM}} \right]^{-1} - \frac{4}{3}G_{HM}, \tag{9}$$

$$G_{dry} = \left[\frac{\frac{1-\Phi}{1-\Phi_c}}{G_{HM} + Z} + \frac{\frac{\Phi-\Phi_c}{1-\Phi_c}}{Z} \right]^{-1} - Z. \tag{10}$$

For porosity Φ lower than Φ_c, K_{dry} and G_{dry} are calculated with the modified lower H-S bound:

$$K_{dry} = \left[\frac{\frac{\Phi}{\Phi_c}}{K_{HM} + \frac{4}{3}G_{HM}} + \frac{1 - \frac{\Phi}{\Phi_c}}{K_g + \frac{4}{3}G_{HM}} \right]^{-1} - \frac{4}{3}G_{HM}, \tag{11}$$

$$G_{dry} = \left[\frac{\frac{\Phi}{\Phi_c}}{G_{HM} + Z} + \frac{1 - \frac{\Phi}{\Phi_c}}{G_g + Z} \right]^{-1} - Z. \tag{12}$$

In both cases, Z is defined as follow:

$$Z = \frac{G_{HM}}{6} \left(\frac{9K_{HM} + 8G_{HM}}{K_{HM} + 2G_{HM}} \right). \tag{13}$$

We then use Gassmann fluid substitution equations (Gassmann, 1951; Mavko et al., 2003) to estimate the effective bulk (K_{sat}) modulus in partial saturation conditions:

$$K_{sat} = K_G \frac{\Phi K_{dry} - (1+\Phi)\frac{K_{fl}K_{dry}}{K_G} + K_{fl}}{(1-\Phi)K_{fl} + \Phi K_G - \frac{K_{fl}K_{dry}}{K_G}}, \tag{14}$$

where K_{fl} is the effective bulk modulus of the fluid and is defined with the Brie's fluid mixing equation (Brie et al., 1995; Wollner & Dvorkin, 2018):

$$K_{fl} = W^e(K_w - K_a) + K_a. \tag{15}$$

The empirical constant e can range between 1 and ∞. In full or partial saturation conditions, the effective shear modulus G_{sat} is identical to the dry effective shear modulus G_{dry}.

Once the effective elastic moduli and density in partial saturation conditions are known, the elastic wave velocities can be calculated as follow:

$$V_P = \sqrt{\frac{K_{sat} + \frac{4}{3}G_{sat}}{\rho_b}} \tag{16}$$

$$V_S = \sqrt{\frac{G_{sat}}{\rho_b}} \tag{17}$$

We performed a preliminary grid search to find the best set of model parameters n, f and e. n ranged between 5 and 20 with steps of 1, f between 0 and 1 with steps of 0.1, and e between 1 and 40 with steps of 1. We minimized a misfit function that incorporates both density and saturation constraints in control points along profile P5. On the one hand, we compare the estimated bulk density in the upper 10 m at the end of P5 ($X = 170$ m; green star in Figure 2 in the main manuscript) with the average density (1000 kg/m^3) measured in a direct sample nearby (Buss et al., 2010). On the other hand, we compare the saturation value estimated in the stream along P5 close to the surface to its expected value $W = 1$ (we expect full saturation there since water was flowing in the stream at the time of the measurements). By minimizing both density and saturation differences, we were eventually able to define the best parameters as $n = 17$, $f = 0.9$ and $e = 24$ (Figure S5) and used them to estimate porosity and saturation along all profiles.

The grid search inversion was then performed on each geophysical profile on cells containing both V_P and V_S information. Porosity and saturation ranged from 0 to 1, with

100 samples following a logarithmic distribution to better sample the strong velocity gradient at high saturation and low porosity. The root-mean-square errors of each profile are summarized in Figure S6. Water saturation uncertainties estimated with the grid search inversions (Figure S8) are low (¡5%), especially in the water-saturated areas of the subsurface, thus reinforcing our confidence in the interpreted water table levels. Porosity uncertainties Figure S8) are also high (about 8% on average), yet they still allow to draw valid interpretations about porosity variations between the main areas of the catchment.

S5. Kriging interpolation

Kriging consists of estimating the unknown value of a variable (i.e., the depth or the elevation) at any point in space using a weighted average of all available observations. The weights given to each data points are based on the spatial correlations and trends that exist within the data set, and also depend on the distance from data points. We first computed an experimental variogram of the data which represents the semivariance (i.e., the average difference of all pairs of data points separated by the same distance) as a function of the distance between these points. A theoretical variogram was then adjusted to fit the experimental variogram in order to describe the data semivariance with a mathematical expression for any distance between points. A more detailed description of the kriging method can be found in Oliver and Webster (2014) and in geostatistics textbooks (e.g., Chilès & Delfiner, 2009).

We followed a four-step procedure to interpolate elevation data of both the water table and the weathering front. This procedure consists in: (i) removing the quadratic trend of the elevation data, (ii) compute the experimental variogram, (iii) test several theoretical variograms, and (iv) apply the best fitting variogram (Oliver & Webster, 2014). We eventually used the super-spherical model (Matern, 1986) as it provided the best fit with experimental variograms of elevation data for both weathering front and water table interpolations (Figure S9). A similar procedure was used to interpolate depth data, with a first step consisting in converting elevation data into depth data by substracting weathering front and water table elevation to the landscape surface topography extracted from the digital elevation model (DEM). We then used ordinary kriging to estimate detrended elevations and depths of both the weathering front and the water table along a regular grid of 10x10 m cells covering the entire watershed. We eventually added the quadratic trend back to the kriged elevations, and the surface elevations back to the kriged depths, so as to obtain two distinct elevation interpolations for both the weathering front and the water table. Following the average kriging methodology proposed by Snyder (2008), we then averaged the results of both interpolations to produce reliable estimates of weathering front and water table elevations in the Quiock watershed (Figure S10). We eventually computed the depth of each interface by removing the landscape surface topography to the interpolated elevations.

References

Bachrach, R., & Avseth, P. (2008, November). Rock physics modeling of unconsolidated sands: Accounting for nonuniform contacts and heterogeneous stress fields in the effective media approximation with applications to hydrocarbon exploration. *Geophysics*, *73*(6), E197–E209. Retrieved from `http://library.seg.org/doi/abs/10.1190/1.2985821` doi: 10.1190/1.2985821

Brie, A., Pampuri, F., Marsala, A. F., & Meazza, O. (1995, October). Shear Sonic Interpretation in Gas-Bearing Sands. OnePetro. Retrieved from https://onepetro.org/SPEATCE/proceedings/95SPE/All-95SPE/SPE-30595-MS/57668 doi: 10.2118/30595-MS

Buss, H. L., White, A. F., Dessert, C., Gaillardet, J., Blum, A. E., & Sak, P. B. (2010). Depth profiles in a tropical, volcanic critical zone observatory: Basse-Terre, Guadeloupe. In *Water-Rock Interaction - Proceedings of the 13th International Conference on Water-Rock Interaction, WRI-13* (pp. 245–248). Retrieved from https://pennstate.pure.elsevier.com/en/publications/depth-profiles-in-a-tropical-volcanic-critical-zone-observatory-b

Chicot, D., Mendoza, J., Zaoui, A., Louis, G., Lepingle, V., Roudet, F., & Lesage, J. (2011, October). Mechanical properties of magnetite (Fe3O4), hematite (α-Fe2O3) and goethite (α-FeO·OH) by instrumented indentation and molecular dynamics analysis. *Materials Chemistry and Physics*, *129*(3), 862–870. Retrieved from http://www.sciencedirect.com/science/article/pii/S0254058411004627 doi: 10.1016/j.matchemphys.2011.05.056

Chilès, J.-P., & Delfiner, P. (2009). *Geostatistics: Modeling Spatial Uncertainty*. John Wiley & Sons. (Google-Books-ID: tZl07WdjYHgC)

Dijkstra, E. W. (1959). A Note on Two Problems in Connexion with Graphs. *Numerische Mathematik*, *1*, 269–271. Retrieved from https://eudml.org/doc/131436

Dunkin, J. W. (1965, January). Computation of modal solutions in layered, elastic media at high frequencies. *Bulletin of the Seismological Society of America*, *55*(2), 335–358.

Retrieved from http://www.bssaonline.org/content/55/2/335

Dvorkin, J., Prasad, M., Sakai, A., & Lavoie, D. (1999). Elasticity of marine sediments: Rock physics modeling. *Geophysical Research Letters*, *26*, 1781–1784. Retrieved from http://adsabs.harvard.edu/abs/1999GeoRL..26.1781D doi: 10.1029/1999GL900332

Gassmann, F. (1951, October). Elastic waves through a packing of spheres. *Geophysics*, *16*(4), 673–685. Retrieved from http://library.seg.org/doi/abs/10.1190/1.1437718 doi: 10.1190/1.1437718

Haskell, N. A. (1953, January). The dispersion of surface waves on multilayered media. *Bulletin of the Seismological Society of America*, *43*(1), 17–34. Retrieved from http://bssa.geoscienceworld.org/content/43/1/17

Hill, R. (1952). The Elastic Behaviour of a Crystalline Aggregate. *Proceedings of the Physical Society. Section A*, *65*(5), 349. Retrieved from http://stacks.iop.org/0370-1298/65/i=5/a=307 doi: 10.1088/0370-1298/65/5/307

Matern, B. (1986). *Spatial Variation* (2nd ed.). New York: Springer-Verlag. Retrieved from https://www.springer.com/gp/book/9781461578925 doi: 10.1007/978-1-4615-7892-5

Mavko, G., Mukerji, T., & Dvorkin, J. (2003). *The Rock Physics Handbook: Tools for Seismic Analysis of Porous Media* (2nd ed.). Cambridge University Press.

Moser, T. (1991, January). Shortest path calculation of seismic rays. *Geophysics*, *56*(1), 59–67. Retrieved from http://library.seg.org/doi/abs/10.1190/1.1442958 doi: 10.1190/1.1442958

Neducza, B. (2007). Stacking of surface waves. *Geophysics*, *72*(2), 51–58. Retrieved from http://link.aip.org/link/?GPY/72/V51/1 doi: 10.1190/1.2431635

Nur, A., Mavko, G., Dvorkin, J., & Galmudi, D. (1998, March). Critical porosity: A key to relating physical properties to porosity in rocks. *The Leading Edge*, *17*(3), 357–362. Retrieved from http://library.seg.org/doi/abs/10.1190/1.1437977 doi: 10.1190/1.1437977

Oliver, M. A., & Webster, R. (2014, February). A tutorial guide to geostatistics: Computing and modelling variograms and kriging. *CATENA*, *113*, 56–69. Retrieved from https://www.sciencedirect.com/science/article/pii/S0341816213002385 doi: 10.1016/j.catena.2013.09.006

O'Neill, A., Dentith, M., & List, R. (2003, January). Full-waveform P-SV reflectivity inversion of surface waves for shallow engineering applications. *Exploration Geophysics*, *34*(3), 158–173. Retrieved from http://www.publish.csiro.au/paper/EG03158

Pasquet, S., & Bodet, L. (2017, July). SWIP: An integrated workflow for surface-wave dispersion inversion and profiling. *Geophysics*, *82*(6), WB47–WB61. Retrieved from http://library.seg.org/doi/abs/10.1190/geo2016-0625.1 doi: 10.1190/geo2016-0625.1

Pasquet, S., Holbrook, W. S., Carr, B. J., & Sims, K. W. W. (2016, December). Geophysical imaging of shallow degassing in a Yellowstone hydrothermal system. *Geophysical Research Letters*, *43*(23), 2016GL071306. Retrieved from http://onlinelibrary.wiley.com/doi/10.1002/2016GL071306/abstract doi: 10.1002/2016GL071306

Pasquet, S., Wang, W., Chen, P., & Flinchum, B. A. (2020, December). Multi-window weighted stacking of surface-wave dispersion. *Geophysics*, *86*(2), EN39–EN50. Retrieved from https://library.seg.org/doi/full/10.1190/geo2020-0096.1 (Publisher: Society of Exploration Geophysicists) doi: 10.1190/geo2020-0096.1

Rücker, C., Günther, T., & Wagner, F. M. (2017, December). pyGIMLi: An open-source library for modelling and inversion in geophysics. *Computers & Geosciences*, *109*, 106–123. Retrieved from http://www.sciencedirect.com/science/article/pii/S0098300417300584 doi: 10.1016/j.cageo.2017.07.011

Sambridge, M. (1999). Geophysical inversion with a neighbourhood algorithm—I. Searching a parameter space. *Geophysical Journal International*, *138*(2), 479–494. Retrieved from http://onlinelibrary.wiley.com/doi/10.1046/j.1365-246X.1999.00876.x/abstract doi: 10.1046/j.1365-246X.1999.00876.x

Snyder, D. T. (2008). Estimated Depth to Ground Water and Configuration of the Water Table in the Portland, Oregon Area.
doi: 10.3133/SIR20085059

Thomson, W. T. (1950, February). Transmission of elastic waves through a stratified solid medium. *Journal of Applied Physics*, *21*(2), 89–93. Retrieved from http://jap.aip.org/resource/1/japiau/v21/i2/p89_s1 doi: doi:10.1063/1.1699629

Wathelet, M., Jongmans, D., & Ohrnberger, M. (2004, November). Surface-wave inversion using a direct search algorithm and its application to ambient vibration measurements. *Near Surface Geophysics*, *2*(4), 211–221. Retrieved from http://

earthdoc.eage.org/detail.php?pubid=8129 doi: 10.3997/1873-0604.2004018

Wollner, U., & Dvorkin, J. (2018). Effective bulk modulus of the pore fluid at patchy saturation. *Geophysical Prospecting*, *66*(7), 1372–1383. Retrieved from http://onlinelibrary.wiley.com/doi/abs/10.1111/1365-2478.12632 (_eprint: https://onlinelibrary.wiley.com/doi/pdf/10.1111/1365-2478.12632) doi: 10.1111/1365-2478.12632

Table S1. Regularization parameters for seismic refraction tomography inversions.

V_{top} (m/s)	V_{bottom} (m/s)	z_{weight}	*lambda*
250	2000	0.25	2
500	3000	0.5	20
750	4000	0.75	200
	5000	1	

Table S2. Elastic parameters for the different minerals found in the regolith

	$K_{mineral}$ (GPa)	$G_{mineral}$ (GPa)	$\rho_{mineral}$ (kg/m^3)
Clays (Mavko et al., 2003)	1.5	1.4	1580
Hydroxides (Chicot et al., 2011)	200	50	5000
Quartz (Mavko et al., 2003)	37	44	2650

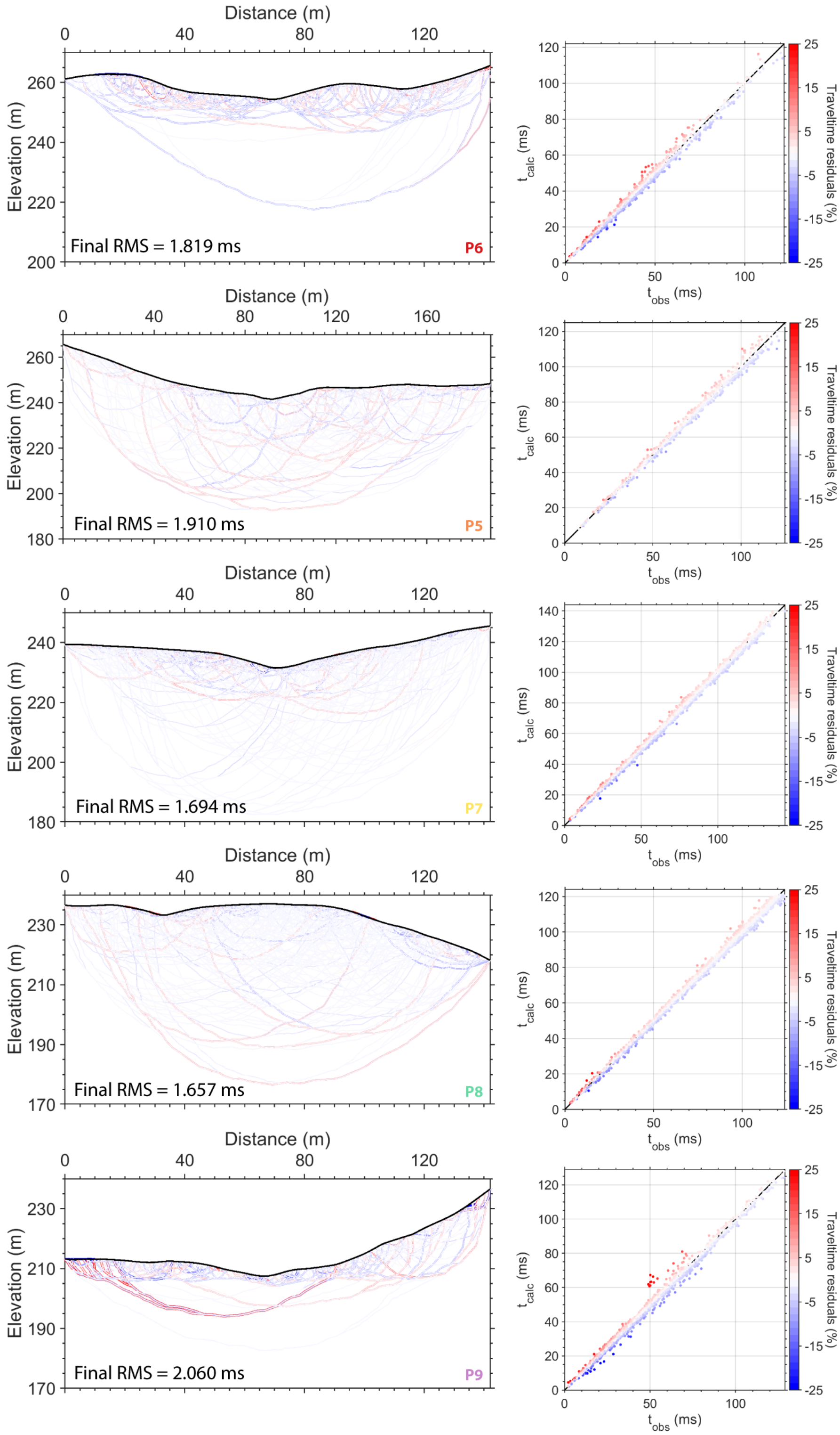

Figure S1. Left column: Raypath distribution for each seismic profile used to mask final V_P models. Right column: Observed vs Calculated traveltimes. The colorscale in both columns corresponds to traveltime residuals (in %).

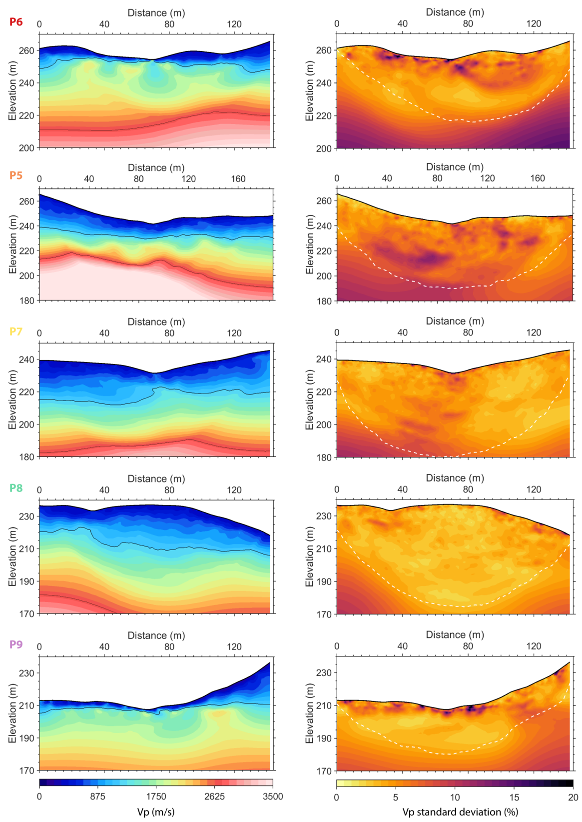

Figure S2. Standard deviation of V_P (in %) computed for each profile from the results of 144 inversions. The white dashed line corresponds to the DOI, estimated from the maximum depth of raypaths (cf Figure S1).

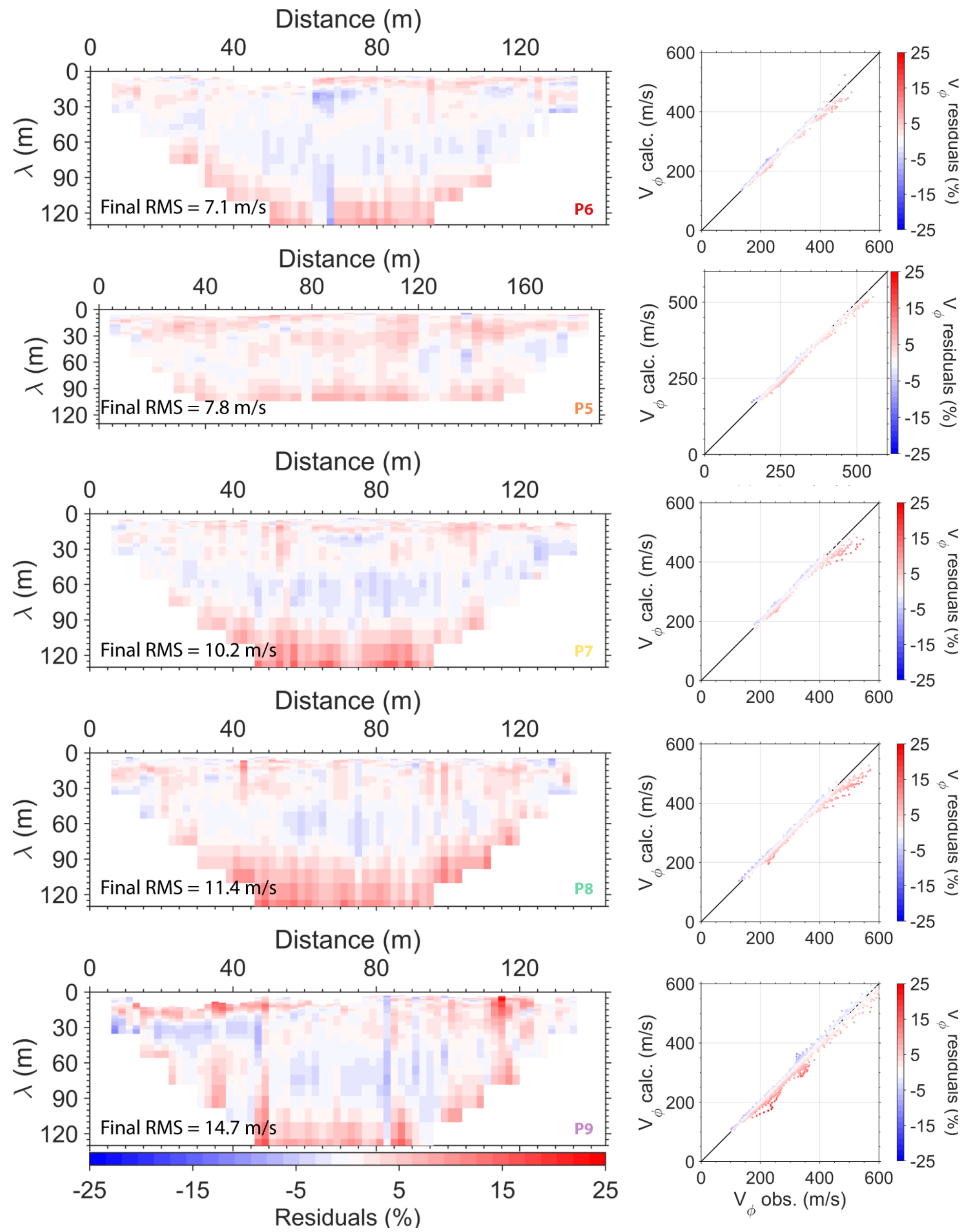

Figure S3. Left column: Phase velocity residuals for each seismic profile. Right column: Observed vs Calculated phase velocities. The colorscale in both columns corresponds to phase velocity residuals (in %).

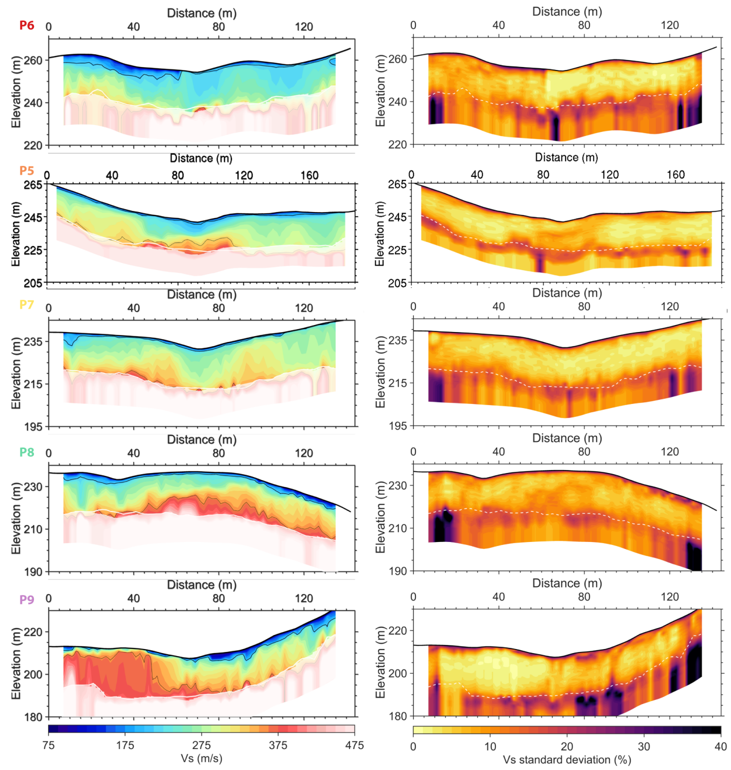

Figure S4. Standard deviation of V_S (in %) computed for each profile from the results of NA inversions. The white dashed line corresponds to the DOI, estimated with a threshold of 15% on the standard deviation.

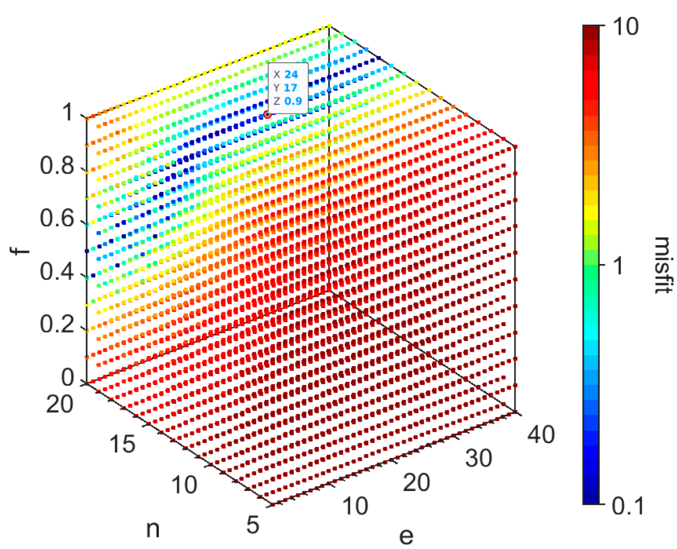

Figure S5. Results of the grid search inversion to determine best parameters for n, f and e.

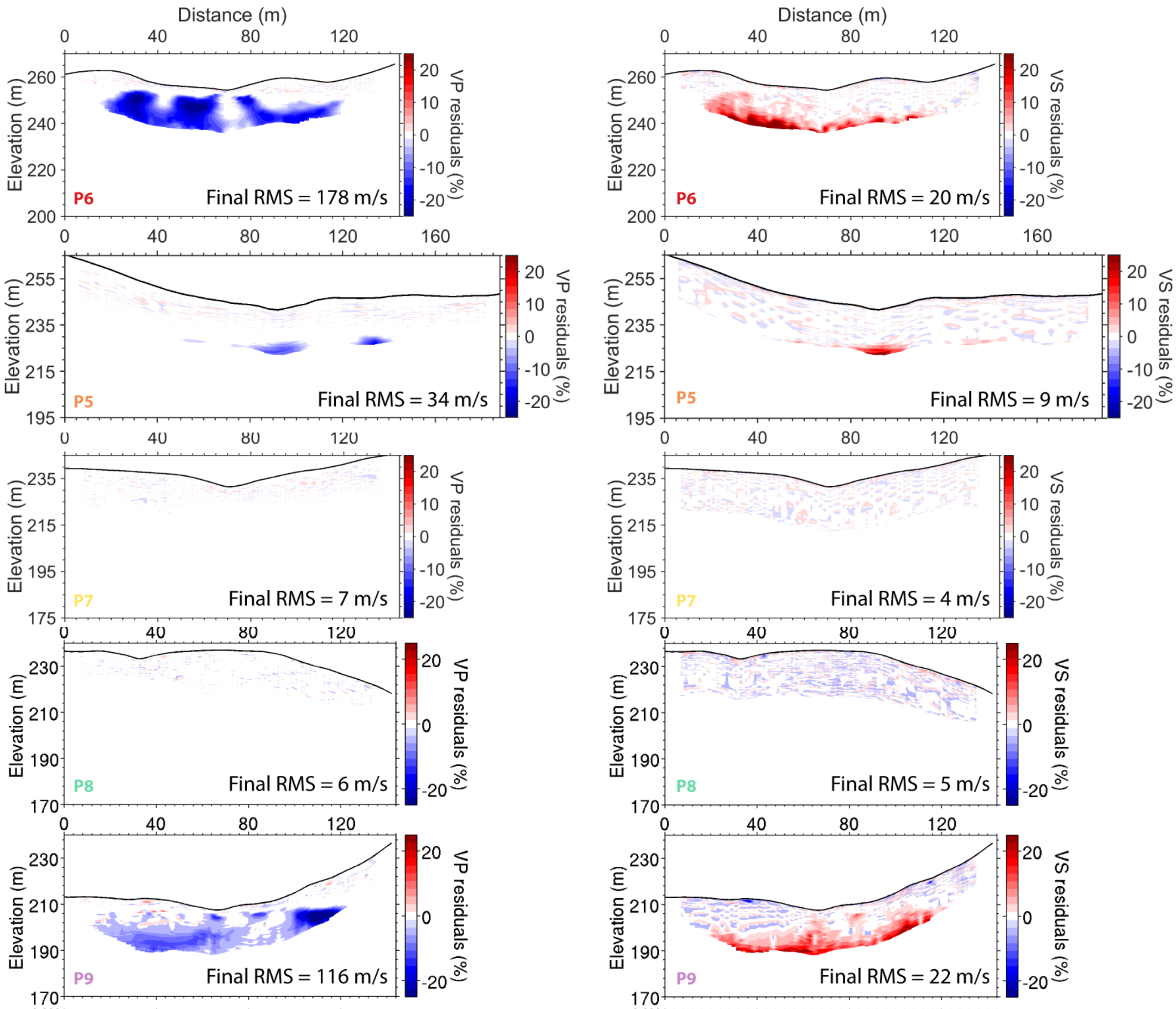

Figure S6. Velocity residuals after the grid search inversion.

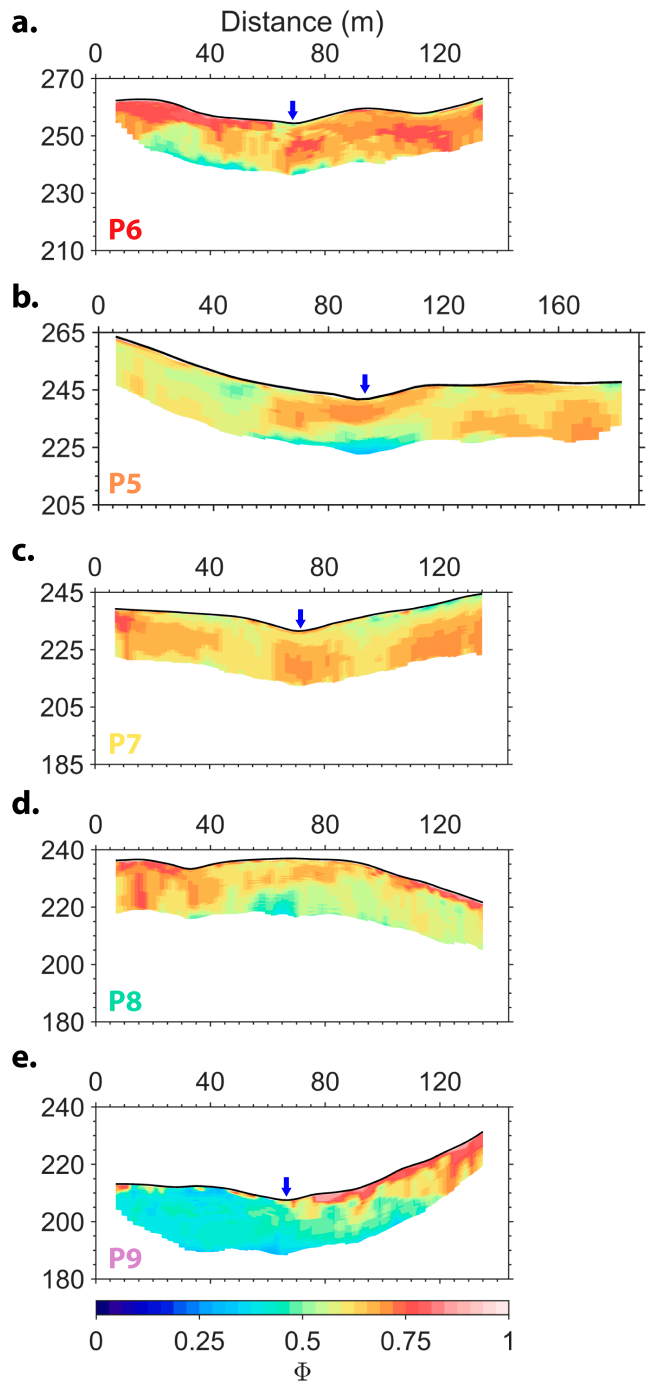

Figure S7. Porosity cross-sections obtained after the grid search inversion.

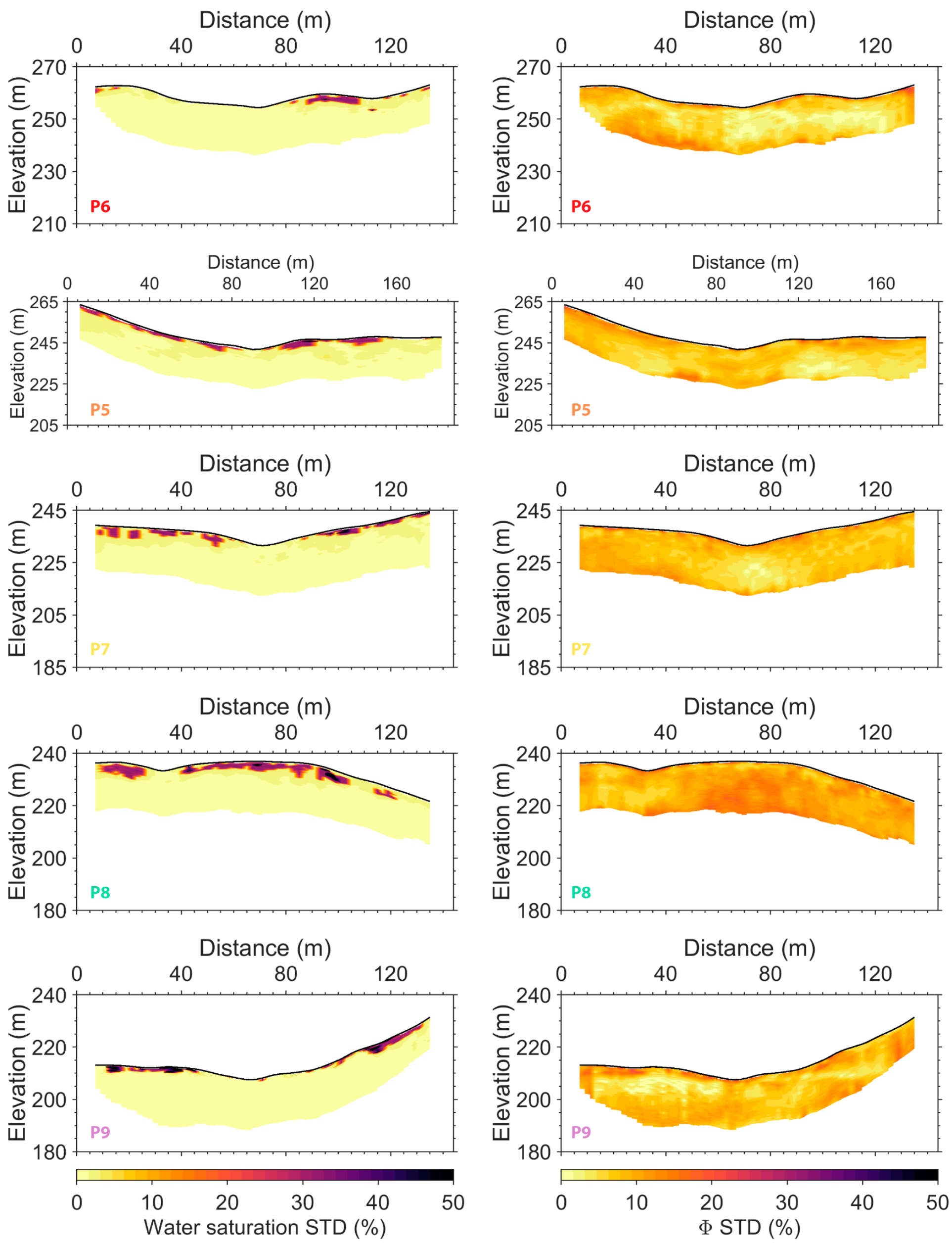

Figure S8. Porosity and saturation uncertainties estimated with the grid search inversion.

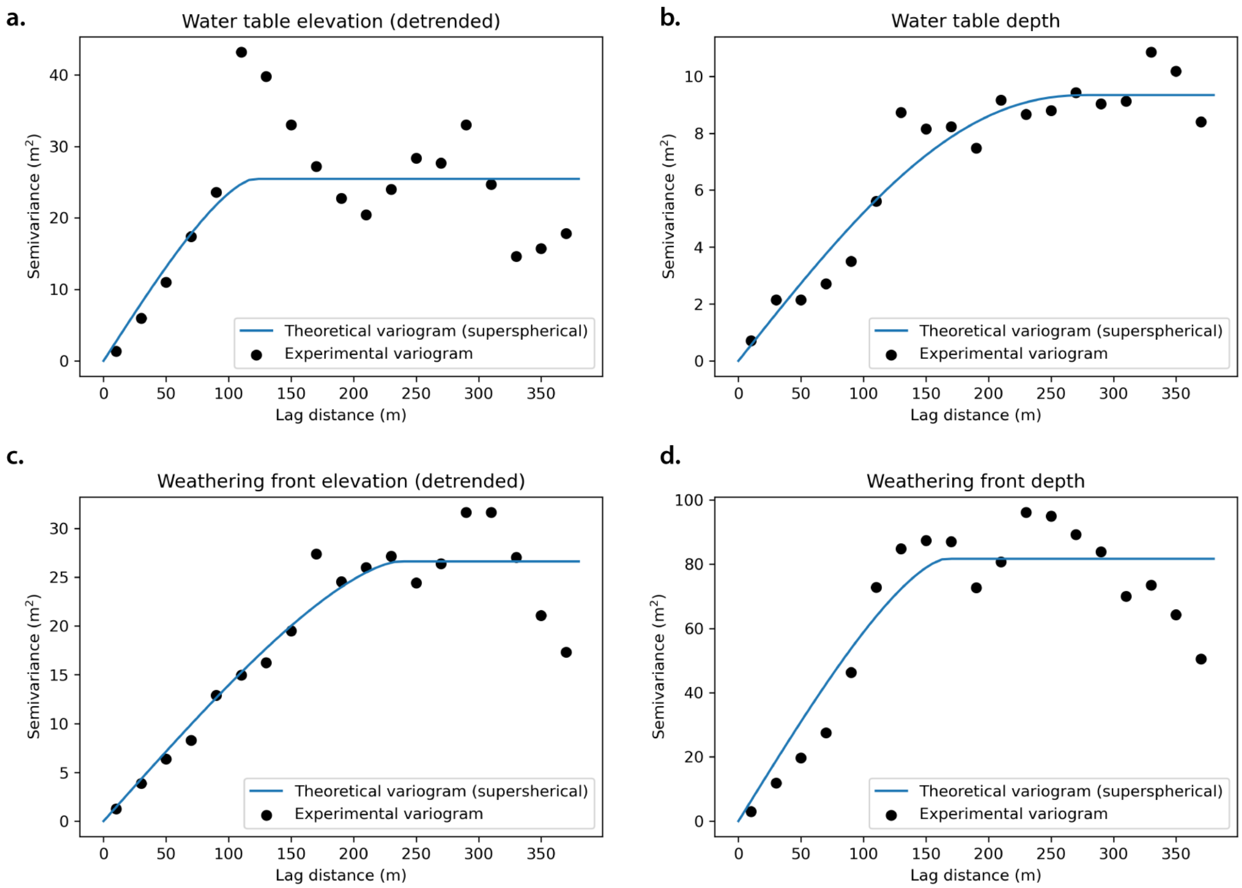

Figure S9. Experimental and theoretical variograms used for interpolating the water table (a) elevation and (b) depth. Experimental and theoretical variograms used for interpolating the weathering front (c) elevation and (d) depth.

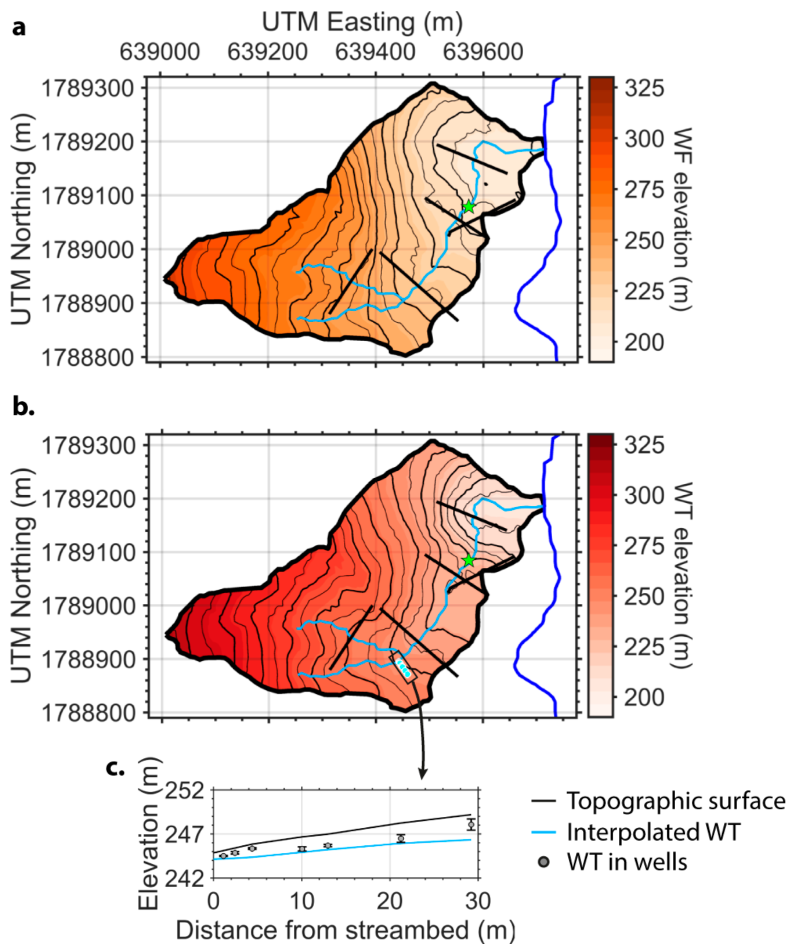

Figure S10. (a) Estimated weathering front (WF) elevation. (b) Estimated water table (WT) elevation. a-b are overlaid with 5-m elevation/depth contours. The extent of the catchment and the seismic lines are shown in black, and the hydrological network in blue. Estimated water table elevations (c) are compared with the mean values observed in the piezometric wells (light blue dots in b) during the geophysical campaign.

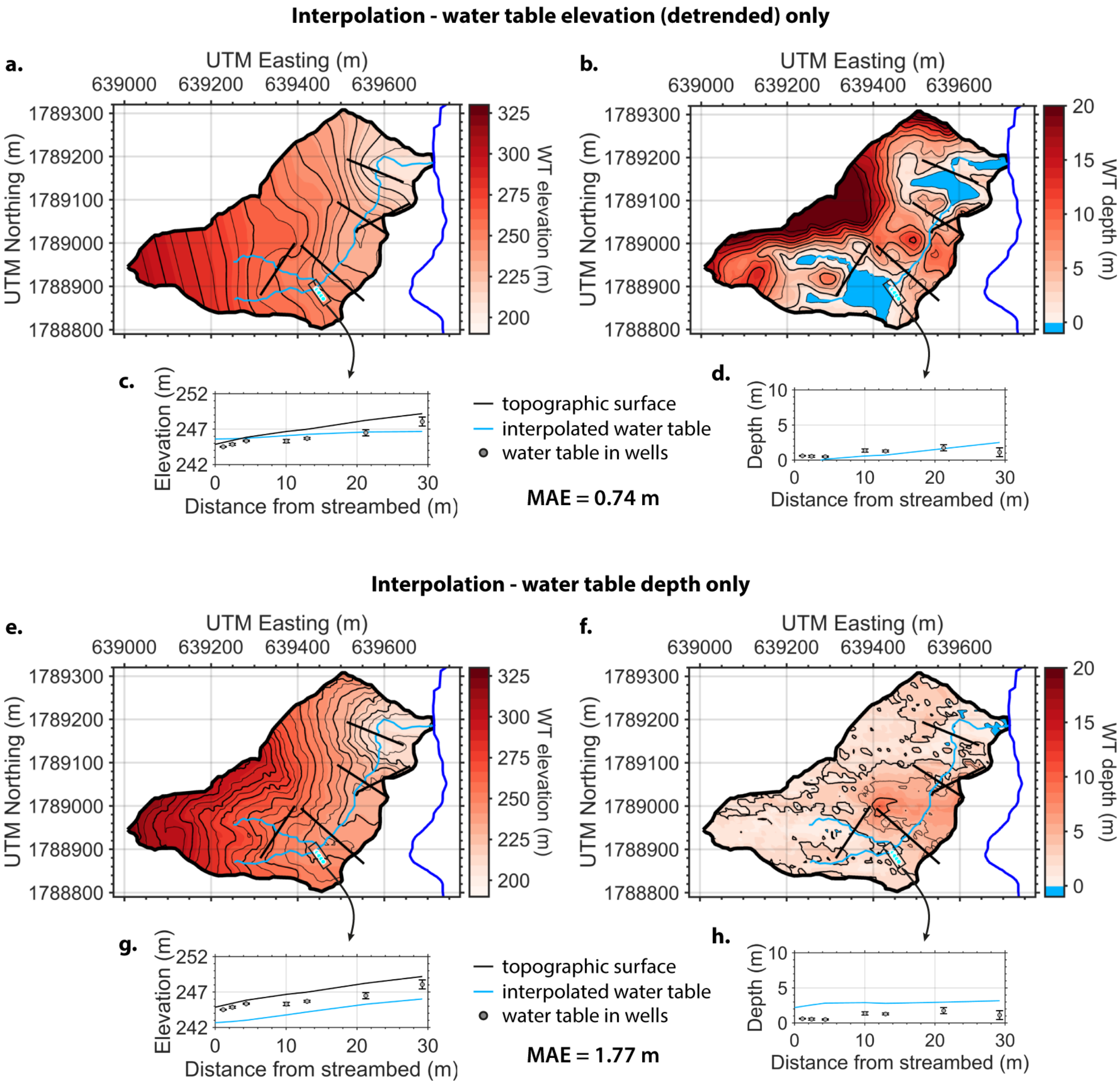

Figure S11. Water table elevation and depth obtained by interpolating detrended water table elevation only (top) and water table depth only (bottom).